

Document reference: IRM/GALOCAD/OUT230-1	Deliverable : OUT230-1	Date: 27-June-2008 Version: 3
Contract ref : GJU/06/2423/CTR/GALOCAD	Written by : G. Wautelet, S. Lejeune, S. Stankov, H. Brenot, R. Warnant	Verified by : R. Warnant

GALOCAD

Development of a Galileo Local Component for the nowcasting and forecasting of atmospheric disturbances affecting the integrity of high precision Galileo applications.

WP 230 Technical Report:

“Effects of small-scale atmospheric activity on precise positioning”

LIST OF ABBREVIATIONS

BDN	Belgian Dense Network
GI/BAS	Geophysical Institute of the Bulgarian Academy of Sciences
GNSS	Global Navigation Satellite System
GPS	Global Positioning System
HDK	Hybrid Dourbes K model
IMF	Interplanetary Magnetic Field
Kd	K index for Dourbes (Belgium)
MAK	Muhtarov Andonov Kutiev model for forecasting Dourbes K
NWP	Numerical Weather Prediction models
RINEX	Receiver Independent Exchange format
RMI	Royal Meteorological Institute
ROB	Royal Observatory of Belgium
RTK	Real Time Kinematics
TEC	Total Electron Content
TECU	TEC Unit
TID	Travelling Ionospheric Disturbance
WEM	Weighted Extrapolation Model
WP	Work Package
ZTD	Zenith Total Delay

TABLE OF CONTENT

List of abbreviations.....	2
Table of Content.....	3
1. Introduction.....	4
2. Atmospheric effects on RTK	5
3. Methodology to assess atmospheric effects on RTK.....	7
4. Quantitative study of the positioning error due to the ionosphere.....	10
5. Correlation between ionospheric residual term and positioning error.....	18
6. Quantitative study of the positioning error due to the neutral atmosphere.....	28
7. Ionospheric effects on aviation.....	33
8. Conclusions.....	48
References.....	50

1 INTRODUCTION

Nowadays, Global Navigation Satellite Systems or GNSS allow to measure positions in real time with an accuracy ranging from a few meters to a few centimetres mainly depending on the type of observable (code or phase measurements) and on the positioning mode used (absolute, differential or relative). In absolute mode, the observer measures his absolute position with only one receiver; the differential mode is a particular case of the absolute mode: the observer still wants to measure his absolute position with only one receiver but he makes use of differential corrections broadcast by a reference station. These corrections allow improving the quality of the measured positions. In relative mode, the observer combines the measurements collected by at least two receivers. The absolute position of one of these two receivers (called reference receiver or reference station) must be known. Based on the combined measurements, it is possible to compute the vector (often called baseline) between the two receivers. Then, the absolute position of the second receiver can be obtained.

The best accuracies can be reached in differential or relative mode using phase measurements. For example, the so-called Real Time Kinematic technique (RTK) allows to measure positions in real time with accuracy usually better than a decimetre. RTK can be used in both differential and relative modes. The level of accuracy obtained mainly depends on the distance between the reference station and the mobile user of whom the position is unknown. Indeed, the RTK technique makes the assumption that the phase measurements made at the reference station and by the mobile user are affected in the same way by most of the error sources: satellite clock and orbit errors, atmospheric effects. In practice, the distance between the reference station and the user is usually smaller than 20 km.

At the present time, atmospheric effects remain the most important error source in high accuracy positioning with the RTK technique. In particular, small-scale variability mainly in the ionospheric plasma but also in the neutral atmosphere can be the origin of strong degradations of RTK accuracy. In the past, many studies have been dedicated to atmospheric effects on real time positioning techniques. Most of them aimed at developing mitigation techniques which allow improving the precision obtained on short distances or aimed at increasing the “acceptable” distance between the stations considered while minimizing the errors. In this report, we develop a method allowing to assess the positioning error which is due to residual atmospheric effects remaining when the mitigation techniques have been applied to the data. The method developed in the frame of this project, does not aim at improving the precision obtained in RTK positioning but it allows to monitor and to quantify the contribution of atmospheric disturbances to the RTK technique error budget.

Applications in aviation are based on carrier-smoothed code observables and also use differential corrections. Therefore, small-scale structures in the ionosphere can also pose a threat for such critical applications. In section 7, we analyze local TEC behaviour induced by the storm of November 20 2003 which could degrade the quality of differential corrections provided by a reference station to an aircraft.

2 ATMOSPHERIC EFFECTS ON RTK

As already stated, the RTK technique can be run both in differential and in relative mode. To fix ideas, we choose to discuss ionospheric effects on RTK used in relative mode: atmospheric disturbances have a similar influence on both positioning modes.

In relative mode, RTK users combine their own phase measurements with the measurements made by a reference station of which the position is precisely known. In practice, the mobile user forms double differences between its own phase measurements and the phase measurements collected in the reference station. In this report, we call receiver A, the reference station receiver, and receiver B, the user receiver.

The simplified mathematical model of phase measurements made by receiver A on satellite i , $\phi_{A,k}^i$ (in cycles of carrier $k = L1$ or $L2$) can be written as follows (Seeber (2003); Leick (2004)):

$$\phi_{A,k}^i = \frac{f_k}{c} \left(D_A^i + T_A^i - I_{A,k}^i + c(\Delta t^i - \Delta t_A) + M_{A,k}^i \right) + N_{A,k}^i + \varepsilon_{A,k}^i \quad (2.1)$$

with:

k , the carrier L1 or L2;

D_A^i , the geometric distance (m) between receiver A and satellite i ;

$I_{A,k}^i$, the ionospheric error (m) on carrier k ;

T_A^i , the tropospheric error (m);

Δt_A , the receiver clock error (the synchronisation error of the receiver time scale with respect to GPS time scale, in seconds) ;

Δt^i , the satellite clock synchronisation error (the synchronisation error of the satellite time scale with respect to GPS time scale, in seconds) ;

$N_{A,k}^i$, the phase ambiguity on carrier k (integer number) ;

$M_{A,k}^i$, multipath effect (m) on carrier k ;

$\varepsilon_{A,k}^i$, noise (cycles) on carrier k ;

f_k , the considered carrier frequency (Hz).

If we neglect higher order terms (terms in f_k^{-3} , f_k^{-4} ...), the ionospheric error $I_{A,k}^i$ is given by:

$$I_{A,k}^i = 40.3 \frac{TEC_A^i}{f_k^2} \quad (2.2)$$

with:

TEC_A^i , the slant TEC from satellite i to receiver A (in electrons/m²).

If $\varphi_{A,k}^i$ and $\varphi_{B,k}^i$ are phase measurements made simultaneously by receivers A and B on satellite i , the single difference $\varphi_{AB,k}^i$ is defined as:

$$\varphi_{AB,k}^i = \varphi_{A,k}^i - \varphi_{B,k}^i \quad (2.3)$$

If receivers A and B observe a second common satellite j , we can form a second single difference $\varphi_{AB,k}^j$. Then, the double difference $\varphi_{AB,k}^{ij}$ is defined as:

$$\varphi_{AB,k}^{ij} = \varphi_{AB,k}^i - \varphi_{AB,k}^j \quad (2.4)$$

Based on equation (2.1), equation (2.4) can be rewritten:

$$\varphi_{AB,k}^{ij} = \frac{f_k}{c} \left(D_{AB}^{ij} + T_{AB}^{ij} - I_{AB,k}^{ij} + M_{AB,k}^{ij} \right) + N_{AB,k}^{ij} + \varepsilon_{AB,k}^{ij} \quad (2.5)$$

with the notation:

$$*_{AB,k}^{ij} = (*_{A,k}^i - *_{B,k}^i) - (*_{A,k}^j - *_{B,k}^j) \quad (2.6)$$

In double differences, all the error sources which are common to the phase measurements performed by receivers A and B cancel, in particular, satellite and receiver clock errors. In addition, in the case of RTK, which is used on short distances, orbit residual errors can be neglected (Seeber, 2003). Indeed, we can compute the ephemeris accuracy needed to measure a baseline of 20 km (maximal acceptable distance in RTK) with an accuracy of 1 cm by using the following formula (Leick 2004):

$$\frac{|db_{AB}|}{|b_{AB}|} = \frac{|dR^i|}{|R_A^i|} \quad (2.7)$$

with :

- db_{AB} and dR^i respectively the error on the baseline length and the error on satellite i position (orbit error) ;
- b_{AB} and R_A^i respectively the baseline vector and the vector linking the satellite i and the receiver A.

If we consider a typical range of 22 000 km between the satellite and the receiver (R_A^i), we find a required ephemeris accuracy of about 11 m. This means that we need satellite positions with accuracy better than 11 m to measure a 20km baseline with 1 cm accuracy. Nowadays, broadcast ephemeris accuracy is about 1.6 m (cf. IGS website); therefore, the orbit residual error can be neglected with respect to the nominal RTK accuracy (which usually ranges between a few cm to about a decimetre for baselines smaller than 10-15 km).

Residual atmospheric effects T_{AB}^{ij} and $I_{AB,k}^{ij}$ depend on the distance between stations A and B and also on the atmospheric “activity”. Given the short distances considered, RTK data processing algorithms assume that residual atmospheric errors are negligible. In this case, neglecting multipath and noise, equation (2.5) can be rewritten:

$$\varphi_{AB,k}^{ij} = \frac{f_k}{c} D_{AB}^{ij} + N_{AB,k}^{ij} \quad (2.8)$$

For the ease of reading, we shall omit the subscript “k” when it is not necessary in the discussion.

In RTK, the position of the reference station (station A) is known by the mobile user (station B). For this reason, the only unknowns which remain in equation (2.8) are the mobile user coordinates X_B, Y_B, Z_B (contained in the term D_{AB}^{ij}) and the ambiguity N_{AB}^{ij} which is an integer number. Let’s assume that five (common) satellites (satellites 1,2,3,4,5) are observed in stations A and B: four independent double differences can be formed $\varphi_{AB}^{12}, \varphi_{AB}^{13}, \varphi_{AB}^{14}, \varphi_{AB}^{15}$. These four equations contain seven unknowns: $X_B, Y_B, Z_B, N_{AB}^{12}, N_{AB}^{13}, N_{AB}^{14}, N_{AB}^{15}$. Therefore, it is not possible to solve all the unknowns using only one observation epoch: RTK needs an initialisation phase. During the initialisation phase, the user remains at the same position during a few minutes so that redundant observations and sufficient information are available to solve (by least squares) the linearised double difference observations for the ambiguities and for the user position. Precise positioning with RTK requires the resolution of the ambiguities N_{AB}^{ij} to the correct integer value in real-time. The ambiguity resolution requires the use of sophisticated techniques like the so-called LAMBDA method (Joosten & Tiberius, 2000). When ambiguities are solved, the user can start to measure precise positions. Equation (2.8) remains a valid mathematical model for double differences as long as residual atmospheric errors remain negligible with respect to GPS carrier wavelength (about 20 cm). This assumption is verified in usual conditions (Leick, 2004). In practice, disturbed meteorological and/or Space Weather conditions can be the origin of small-scale (a few kilometres) atmospheric variability which can itself strongly degrade or even prevent ambiguity resolution due to the fact that, in that case, the mathematical model given by equation (2.8) does not adequately represent the observed double differences.

The meteorological and Space Weather conditions which are the origin of the occurrence of small-scale structures in the atmosphere have been characterized in details in WP 250 and WP 220 reports.

3 METHODOLOGY TO ASSESS ATMOSPHERIC EFFECTS ON RTK

In order to have a realistic quantitative assessment of the ionospheric influence on RTK accuracy, we decided to develop software based on the technique used in RTK to compute real time positions on the field. This technique has been described in paragraph 2. The idea is to reproduce as close as possible the “positioning conditions” that RTK

users undergo on the field. Nevertheless, it is very clear that each observation site is different and that it will never be possible to reproduce exactly the conditions encountered by each user. This software uses GPS stations from the Belgian Dense Network to play the role of reference station (station A) and mobile station (station B). The position of these stations is known at a few mm level. As the “nominal” RTK accuracy is a few cm, we will consider that the position of these permanent stations is perfectly known and we will refer to it as the “true” station position.

The most difficult point is to be able to isolate the part of the user position error budget which is due only to the ionosphere or to the neutral atmosphere. In order to achieve this goal, data are processed in 5 steps.

3.1. Resolution of L1 and L2 ambiguities and computation of the term

$$I_{AB,GF}^{ij}$$

In WP 220 paragraph 5, we have outlined the strategy we are using to compute TEC_{AB}^{ij} (which allows to obtain $I_{AB,k}^{ij}$) and to solve the L1 and L2 double difference integer ambiguities $N_{AB,k}^{ij}$. The same strategy is applied here. During this step, our software forms double differences based on the L1 and L2 phase measurements collected on all the satellites in view in stations A and B. Then ambiguities $N_{AB,L1}^{ij}$ and $N_{AB,L2}^{ij}$ are solved based on double differences of the wide lane and of the geometric free combinations; these ambiguities are not solved on periods of a few minutes as it is the case “on the field” but using all the available data for the considered satellite pair. When the ambiguities are solved, the term TEC_{AB}^{ij} can be computed from double differences of the geometric free combination neglecting multipath and noise (see WP 220 report equations 5.6 and 5.8):

$$\varphi_{AB,GF}^{ij} - N_{AB,GF}^{ij} = 0,552 \cdot 10^{-16} TEC_{AB}^{ij} + M_{AB,GF}^{ij} + \varepsilon_{AB,GF}^{ij} \quad (3.1)$$

Then $I_{AB,k}^{ij}$ can be obtained from TEC_{AB}^{ij} :

$$I_{AB,k}^{ij} = 40.3 \frac{TEC_{AB}^{ij}}{f_k^2} \quad (3.2)$$

Let’s underline that, in practice, the term $I_{AB,k}^{ij}$ obtained by this method also contains the influence of multipath and noise.

3.2. Computation of the user position (station B)

The user position can be computed from the linearised equation (2.5) where it is assumed that all error terms (T_{AB}^{ij} , $I_{AB,k}^{ij}$, $M_{AB,k}^{ij}$) are negligible and where double differences are corrected for the ambiguity (solved during step 1):

$$\varphi_{AB,k}^{ij} - N_{AB,k}^{ij} = \frac{f_k}{c} \left(D_{AB}^{ij} + T_{AB}^{ij} - I_{AB,k}^{ij} + M_{AB,k}^{ij} \right) + \varepsilon_{AB,k}^{ij} \quad (3.3)$$

The position is obtained from a least square adjustment involving 5 minute periods of measurements. In practice, the positions computed during this step are still affected by all error terms. We shall refer to these positions as: $X_{B,1}$, $Y_{B,1}$, $Z_{B,1}$.

3.3. Computation of the user position based on double difference corrected for the ionospheric effect

Double differences $\varphi_{AB,k}^{ij}$ are corrected for the ambiguity and for the ionospheric term $I_{AB,k}^{ij}$ obtained during step 1:

$$\varphi_{AB,k}^{ij} + \frac{f_k}{c} I_{AB,k}^{ij} - N_{AB,k}^{ij} = \frac{f_k}{c} \left(D_{AB}^{ij} + T_{AB}^{ij} + M_{AB,k}^{ij} \right) + \varepsilon_{AB,k}^{ij} \quad (3.4)$$

The user position can be computed again from these double differences corrected for the ionosphere (equation (3.4)) where it is assumed that all remaining error terms (T_{AB}^{ij} , $M_{AB,k}^{ij}$) are negligible. In a similar way as it has been done in step 2, the position is obtained from a least square adjustment involving 5 minute periods of measurements. We shall refer to these positions as: $X_{B,2}$, $Y_{B,2}$, $Z_{B,2}$. From equation (3.4), we see that they do not depend on the ionospheric effects but they still depend on T_{AB}^{ij} , $M_{AB,k}^{ij}$, noise and also on satellite geometry. In fact, taking into account the way it is computed, the term $I_{AB,k}^{ij}$ also contains multipath. Therefore, we can consider that these double differences corrected for $I_{AB,k}^{ij}$ are also corrected for (a part of) multipath. Nevertheless, as the magnitude of ionospheric effects is usually much larger than the magnitude of multipath, we shall consider that the difference between ($X_{B,1}$, $Y_{B,1}$, $Z_{B,1}$) and ($X_{B,2}$, $Y_{B,2}$, $Z_{B,2}$) is mainly due to the ionosphere.

3.4. Computation of the positioning error due to the ionosphere

The absolute value of the difference between ($X_{B,1}$, $Y_{B,1}$, $Z_{B,1}$) and ($X_{B,2}$, $Y_{B,2}$, $Z_{B,2}$) is computed. We select this parameter to assess the influence of the ionosphere on RTK

positions. Indeed, it allows to “isolate” the influence of the ionosphere from the other error sources. This difference can be transformed into horizontal and vertical components (north, east, up) and will be referred to as $(\Delta N_{\text{iono}}, \Delta E_{\text{iono}}, \Delta U_{\text{iono}})$.

3.5. Computation of the positioning error due to the troposphere

From the discussion above, it comes that $(X_{B,2}, Y_{B,2}, Z_{B,2})$ still depends on tropospheric effects, geometry, residual multipath and noise. Therefore, we shall assess the influence of the troposphere on RTK positions by computing the absolute value of the difference between the “true” position and the computed position $(X_{B,2}, Y_{B,2}, Z_{B,2})$. Nevertheless, it is important to underline that this strategy has a disadvantage: not only disturbed tropospheric conditions can be the origin of large differences between these positions; for example, bad satellite coverage could also be the origin of “out of tolerance” errors. We will have to take this point into account during our discussion about tropospheric effects.

4 QUANTITATIVE STUDY OF THE POSITIONING ERROR DUE TO THE IONOSPHERE

4.1. Presentation of the cases studies and methodology

In this paragraph, we will analyse the same cases than in WP 220: 5 baselines and 4 different days. The baselines are the following ones (figure 4.1):

- GILL – LEEU (11.3 km)
- GILL – MECH (20.5 km)
- OUDE – GERA (19.9km)
- OUDE – ZVEW (19.4 km)
- OUDE – GENT (18.7 km)

The selected days for the analysis are:

- Quiet day: 103/07 ;
- Day with medium-amplitude TID: 359/04, satellite pair 5/6 (9.725h – 9.966h) ;
- Day with large-amplitude TID: 301/03, satellite pair 7/5 (11.33h – 11.575h) ;
- Day with severe geomagnetic storm: 324/03, satellite pair 16/2 (17.358h – 17.608h).

Let us recall that the periods described above were chosen on the basis of the results obtained from the one-station method. Indeed, these selected periods correspond to time intervals where RoTEC values and variability (for a given satellite) were representative of the “typical cases” we wanted to analyze: quiet ionosphere, TID or geomagnetic storm.

In WP 220, these periods have been processed and analyzed with the double difference software in order to quantify the effects of the residual ionosphere on specific satellite pairs during these typical ionospheric conditions. The outputs of this analysis were values of the ionospheric residual term related to given satellite pairs.

In this section, the goal is to assess the influence of these specific double differences in terms of positioning error. As the least-square process needs at least 3 different satellite pairs to compute the positioning error (if the ambiguities are solved), we can not affirm that those analyzed periods, which correspond to typical cases in terms of RoTEC, induce automatically the worst positioning error values for the whole considered day. Indeed, the other satellite pairs involved in the least-square process could be less “affected” by the ionospheric effects.

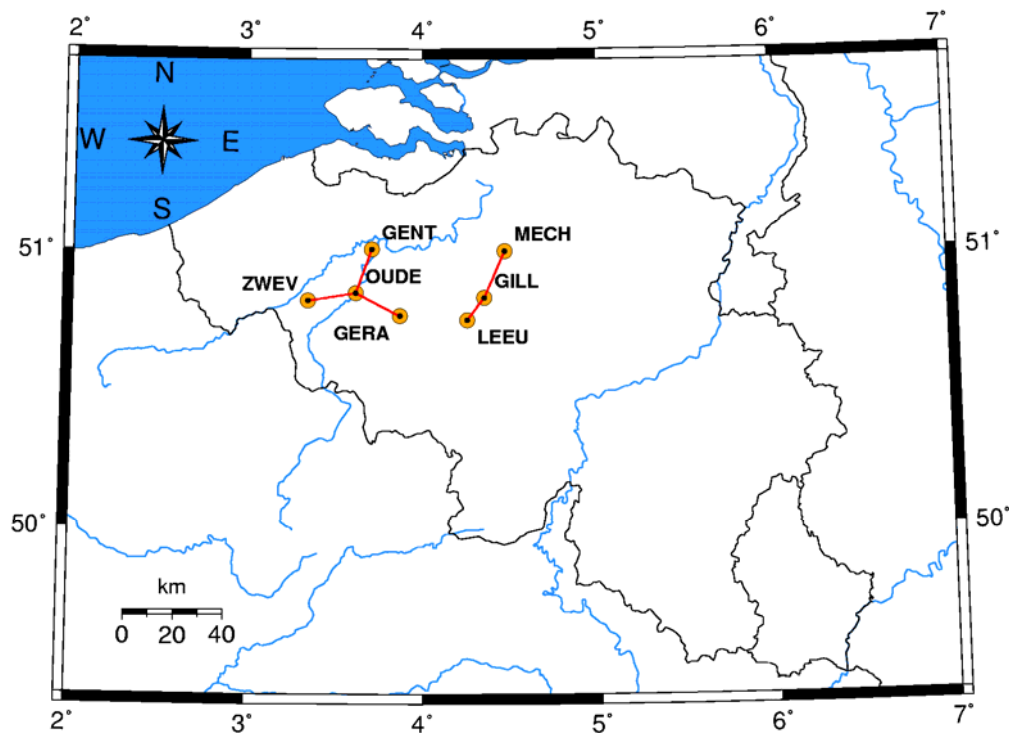


Figure 4.1. Selected baselines

As explained in section 3, the positioning error due to the ionosphere (ΔN_{iono} , ΔE_{iono} , ΔU_{iono}) is computed on 5 minute periods. For each 15 minute interval, we obtain only 3 positioning errors per baseline, which is too few to make Fisher’s test like in WP 220 to assess the influence of the baseline length or orientation on the positioning error due to ionospheric residual term. However, we will extract some quantitative statistics about the positioning error to assess of the error distribution among the different baselines.

4.2. Quiet day: 103/07

In order to characterize a quiet ionospheric day, we have chosen to use the 288 positioning errors (ΔN_{iono} , ΔE_{iono} , ΔU_{iono}) relative to the 24 hours of the day (periods of 5 minutes).

We compute the mean and the standard deviation for each baseline and each component; these values expressed in meters are shown in table 1.

	North		East		Up	
	Mean [m]	Sd [m]	Mean [m]	Sd [m]	Mean [m]	Sd [m]
GILL - LEEU	0.0051	0.0035	0.0032	0.0022	0.0068	0.0060
GILL - MECH	0.0061	0.0048	0.0029	0.0023	0.0085	0.0072
OUDE - GERA	0.0069	0.0067	0.0050	0.0043	0.0100	0.0099
OUDE - ZWEV	0.0048	0.0045	0.0053	0.0038	0.0090	0.0081
OUDE - GENT	0.0080	0.0055	0.0030	0.0030	0.0082	0.0067

Table 1. Positioning error due to the ionosphere considering 24h of data; quiet day in terms of ionospheric variability (DOY 103/07).

Table 1 allows us to quantify the “nominal” positioning error due to the ionosphere on a given baseline; as we have four baselines having a similar length (GILL-MECH, OUDE-GERA, OUDE-ZWEV and OUDE-GENT), we can compute the mean of the positioning error to quantify the effect of the ionospheric residual error during a quiet ionospheric day. Moreover, we can extract from these four 20 km baselines the maximum and minimum values of the positioning error due to the ionosphere for each of the three components (table 2).

	North [m]	East [m]	Up [m]
Mean	0.0064	0.0040	0.0089
Min	0.0000	0.0000	0.0000
Max	0.0299	0.0260	0.0545

Table 2. Mean, minimum and maximum of the positioning error due to the ionosphere for the four 20 km baselines (DOY 103/07).

The analysis of table 2 shows that the mean positioning error due to the ionosphere ranges from about 4 to 9 mm for a 20 km baseline, depending on the considered component. Maximum positioning errors range from about 25 mm to 55 mm; these values are not “out of tolerance” with respect to the typical accuracy of the RTK technique. Indeed, we consider that RTK allows to measure positions with an accuracy ranging from a few centimetres to about a decimetre during standard conditions for baselines smaller than 10-15 km.

In conclusions, tables 1 & 2 show that positioning error due to the ionosphere for a 20 km baseline is less than 1 cm on average but can reach more that 5 cm.

4.3. Day with medium-amplitude TID: 359/04

The selected 15 minute interval where the TID occurred allows us to extract the positioning error due to the ionosphere every 5 minutes for each of the components; the results are shown in table 3.

By comparing the values shown in table 3 with the values relative to the quiet day (see tables 1 & 2), we can say that a major part of the positioning errors during the occurrence of this TID is larger than the mean positioning error observed during the quiet day 103/07. From table 3, we can also say that the TID of DOY 359/04 induces a positioning error which is distributed on each component during the least-square process.

	GPS Time (5min steps) [h]	North [m]	East [m]	Up [m]
GILL – LEEU	9.750	0.0024	0.0158	0.0135
	9.833	0.0155	0.0026	0.0124
	9.917	0.0108	0.0133	0.0078
GILL – MECH	9.750	0.0117	0.0059	0.0474
	9.833	0.0070	0.0027	0.0198
	9.917	0.0102	0.0196	0.0065
OUDE - GERA	9.750	0.0134	0.0047	0.0267
	9.833	0.0034	0.0088	0.0027
	9.917	0.0029	0.0163	0.0131
OUDE - ZWEV	9.750	0.0048	0.0002	0.0080
	9.833	0.0168	0.0306	0.0185
	9.917	0.0172	0.0187	0.0048
OUDE – GENT	9.750	0.0346	0.0289	0.0200
	9.833	0.0229	0.0044	0.0112
	9.917	0.0114	0.0272	0.0350

Table 3. Positioning error due to the ionosphere during the TID of DOY 359/04.

Moreover, the analysis of table 3 shows that, for a similar baseline orientation (*i.e.* GILL-LEEUE and GILL-MECH baselines), we cannot state that the positioning error due to the occurrence of the TID is smaller for the smaller baseline than for the other one. Let us recall that table 3 contains results obtained during a 15 minute period, which is not necessarily representative of the positioning error experienced during the whole day. Further investigations and more data are necessary to establish a relationship between the baseline length and the positioning error due to the ionosphere (see section 5).

Nevertheless, considering the four baselines of about 20 km length, we can compute the descriptive statistics that are the mean, the minimum and the maximum of the positioning error for each of the five minute interval (tables 4 & 5).

Table 5 shows that for the same time interval and the same component, the positioning errors can be very different from a baseline to another because minimum and maximum values are very far from each other. For example, during the time interval of 9.750 h, the positioning error on the north component ranges between 5 mm and 35 mm, depending on the considered baseline.

GPS Time (5min steps) [h]	North [m]	East [m]	Up [m]
9.750	0.0162	0.0099	0.0255
9.833	0.0100	0.0093	0.0104
9.917	0.0104	0.0205	0.0148

Table 4. Mean of the positioning error due to the ionosphere on the four 20 km baselines during the occurrence of the TID of DOY 359/04.

GPS Time (5min steps) [h]	North		East		Up	
	MIN [m]	MAX [m]	MIN [m]	MAX [m]	MIN [m]	MAX [m]
9.750	0.0048	0.0346	0.0002	0.0289	0.0080	0.0474
9.833	0.0034	0.0229	0.0027	0.0306	0.0027	0.0198
9.917	0.0029	0.0172	0.0163	0.0272	0.0048	0.0350

Table 5. Maximum and minimum positioning errors due to the ionosphere on the four 20 km baselines during the occurrence of the TID of DOY 359/04.

Finally, the effects of the medium-amplitude TID of DOY 359/04 on positioning error due to the ionosphere seem to depend mainly on baseline orientation and on the considered component. The observed positioning error due to ionosphere ranges between less than 1 mm and about 5 cm. The maximum error due to the medium-amplitude TID on DOY 359/04 during the considered 15 minute time interval is of the same order of magnitude than the maximum error experienced during the quiet day. Therefore, further investigation based on more data is necessary (see section 5).

4.4. Day with large-amplitude TID: 301/03

We can use the same reasoning than for the section 4.3 to analyze the effect of a large-amplitude TID on the positioning error due to the ionosphere (table 6).

	GPS Time (5min steps) [h]	North [m]	East [m]	Up [m]
GILL - LEEU	11.333	0.0296	0.0346	0.0246
	11.417	0.0466	0.0002	0.0193
	11.500	0.0436	0.0073	0.0280
GILL - MECH	11.333	0.0134	0.1070	0.0171
	11.417	0.0573	0.0354	0.0844
	11.500	0.0633	0.0005	0.1484
OUDE - GERA	11.333	0.0539	0.0272	0.0390
	11.417	0.0089	0.0812	0.1460
	11.500	0.0028	0.0524	0.0414
OUDE - ZWEV	11.333	0.0669	0.0241	0.0574
	11.417	0.0227	0.0530	0.1155
	11.500	0.0215	0.0018	0.0423
OUDE - GENT	11.333	0.0090	0.0384	0.0882
	11.417	0.0209	0.0157	0.0852
	11.500	0.0335	0.0379	0.0254

Table 6. Positioning error due to the ionosphere during the TID of DOY 301/03.

As for the day 359/04, we can also compute the mean, the maximum and minimum values of the positioning error for each time period and each component for the four baselines considered (tables 7 & 8).

GPS Time (5min steps) [h]	North [m]	East [m]	Up [m]
11.333	0.0358	0.0492	0.0504
11.417	0.0219	0.0370	0.0862
11.500	0.0303	0.0232	0.0644

Table 7. Mean of the positioning error due to the ionosphere on the four 20 km baselines during the occurrence of the TID of DOY 301/03.

GPS Time (5min steps) [h]	North		East		Up	
	MIN [m]	MAX [m]	MIN [m]	MAX [m]	MIN [m]	MAX [m]
11.333	0.0090	0.0669	0.0241	0.1070	0.0171	0.0882
11.417	0.0089	0.0573	0.0157	0.0812	0.0844	0.1460
11.500	0.0028	0.0633	0.0005	0.0524	0.0254	0.1484

Table 8. Maximum and minimum positioning errors due to the ionosphere on the four 20 km baselines during the occurrence of the TID of DOY 301/03.

When considering the results shown in tables 6 to 8 and by following the same reasoning than in section 4.3 to analyze the data, the conclusions are quite similar than in the case of the medium-amplitude TID:

- Baseline length does not seem to have an influence on the magnitude of the positioning error due to the ionosphere. Indeed, the positioning error values are sometimes smaller and sometimes larger for the smaller baseline GILL-LEEUE (11.3 km). This effect could be due to the physical properties of the TID (wavelength, speed, spatial extent...).
- The positioning error fluctuates very strongly from a component to another.
- The positioning error fluctuates very strongly from a baseline to another.

Nevertheless, we can say that the mean and the maximum values are larger for the large-amplitude TID (around 15 cm) than for the medium-amplitude TID (around 5 cm) and for the quiet day (around 5 cm). Indeed, when having a look at tables 4, 5, 7 & 8 we clearly see that mean and standard deviation values are larger during the occurrence of the large-amplitude TID.

Finally, we can conclude that during the occurrence of the TID of DOY301/03, the positioning error due to the ionosphere ranges between less than 1 mm and about 15 cm.

4.5. Day with geomagnetic storm: 324/03

As in section 4.4, we use the same methodology to assess the effects of a severe geomagnetic storm on the positioning error due to the ionosphere (tables 9 to 11).

The conclusions that we can formulate on the basis of tables 9 to 11 are also the same as for the previous sections (see sections 4.3 & 4.4).

However, the smaller baseline GILL-LEEUE (11.3 km) seems to be a little less disturbed than the baseline GILL-MECH (20.5 km) which has the same orientation. Indeed, from table 9 we can observe that nearly all values of the positioning error are larger for the 20 km baseline than for the 11 km baseline. Nevertheless, we need to analyze more data to confirm the assumption that, in case of geomagnetic storm, the positioning error induced by the ionosphere increases with increasing baseline length (see section 5).

Tables 10 & 11 allow us to quantify the positioning error for a typical 20 km baseline. We can see that these values are generally larger than the values obtained for the DOY 301/03 (tables 7 & 8) and, a fortiori, than the values of DOY 359/04 and 103/07.

	GPS Time (5min steps) [h]	North [m]	East [m]	Up [m]
GILL - LEEU	17.333	0.0392	0.0048	0.0127
	17.417	0.0690	0.0091	0.0540
	17.500	0.0006	0.0795	0.0264
GILL - MECH	17.333	0.3143	0.0469	0.3190
	17.417	0.2799	0.0247	0.3622
	17.500	0.0052	0.0099	0.0526
OUDE - GERA	17.333	0.1130	0.0257	0.1728
	17.417	0.1893	0.0388	0.1963
	17.500	0.0980	0.0563	0.1531
OUDE - ZWEV	17.333	0.0107	0.0084	0.0827
	17.417	0.0726	0.0514	0.1171
	17.500	0.1155	0.0037	0.3264
OUDE - GENT	17.333	0.0408	0.0832	0.0008
	17.417	0.0543	0.0573	0.0054
	17.500	0.0209	0.0509	0.2517

Table 9. Positioning error due to the ionosphere during the geomagnetic storm of DOY 324/03.

GPS Time (5min steps) [h]	North [m]	East [m]	Up [m]
17.333	0.1197	0.0410	0.1438
17.417	0.1192	0.0344	0.1362
17.500	0.0599	0.0302	0.1959

Table 10. Mean of the positioning error due to the ionosphere on the four 20 km baselines during the occurrence of the geomagnetic storm of DOY 324/03.

GPS Time (5min steps) [h]	North		East		Up	
	MIN [m]	MAX [m]	MIN [m]	MAX [m]	MIN [m]	MAX [m]
17.333	0.0107	0.3143	0.0084	0.0832	0.0008	0.3190
17.417	0.0543	0.2799	0.0247	0.0573	0.0054	0.3622
17.500	0.0052	0.1155	0.0037	0.0563	0.0526	0.3264

Table 11. Maximum and minimum values of the positioning error due to the ionosphere on the four 20 km baselines during the occurrence of the geomagnetic storm of DOY 324/03.

Finally, we can conclude that, during the considered 15 minute interval, the effects of the severe geomagnetic storm which occurred on DOY 324/03 on the positioning error depend on the baseline orientation and on the baseline length. Positioning error due to the ionosphere ranges between 1 mm and 36 cm.

4.6. Conclusions

In this section we quantified the positioning error due to the ionosphere during several typical ionospheric conditions selected on the basis of RoTEC values obtained with the one-station method. The analyzed periods, except for the quiet day, correspond to 15 min time intervals during which the ionospheric variability was typical of the studied phenomenon as “seen” by a given satellite pair: TID or geomagnetic storm. We observed that, even though the amount of data was not very large, positioning error was very different from a baseline to another, even for a similar baseline length.

Moreover, we quantified the mean and the maximum value of the positioning error due to the ionosphere for a quiet day in terms of ionospheric variability. For a 20 km baseline, the mean error is smaller than 1 cm but can reach 5 cm.

Finally, we quantified the maximum positioning error due to the ionosphere during different disturbed conditions considered as typical cases (periods of 15 minutes); these maximum values are for a 20 km baseline:

- Medium-amplitude TID: ~ 5 cm ;
- Large-amplitude TID: ~ 15 cm ;
- Severe geomagnetic storm: ~ 36 cm.

5 CORRELATION BETWEEN IONOSPHERIC RESIDUAL TERM AND POSITIONING ERROR

5.1. Methodology

In this section, we analyze the relationship between the ionospheric residual term $I_{AB,GF}^{ij}$ and the positioning error due to the ionosphere. This study will be made on the basis of plots of these two variables in function of time; the data relative to the whole day are represented (*i.e.* 24 hours).

We compute the positioning error due to the ionosphere every 5 minute interval; this error, called ΔD_{iono} , is defined as follows:

$$\Delta D_{iono} = \sqrt{\Delta N_{iono}^2 + \Delta E_{iono}^2 + \Delta U_{iono}^2} \quad (5.1)$$

with ΔN_{iono} , ΔE_{iono} , ΔU_{iono} respectively the north, east and up components of the positioning error due to ionosphere as defined in section 3.4.

The term $I_{AB,GF}^{ij}$ which is computed every 30 s is plotted for all the satellite pairs in view; that means that several different values of $I_{AB,GF}^{ij}$ are plotted simultaneously. Therefore, the plots will show the “envelope” of these simultaneous values. Let us recall that the computed position is the result of a least-square process which involves all the satellites in view. Therefore, the “envelope” of $I_{AB,GF}^{ij}$ should be representative of the positioning error due to the ionosphere.

For each of the analyzed days, the graphs will be laid out on a page which contains four plots relative to the following baselines: GILL-LEEUE, GILL-MECH, OUDE-ZWEV and OUDE-GENT. Unfortunately, we experienced failures in ambiguity resolution which gave outliers and offsets in $I_{AB,GF}^{ij}$ on baseline OUDE-GERA. Further refinement of our ambiguity resolution technique is necessary to fix this problem. For this reason, we will not show the results relative to the baseline OUDE-GERA.

The positioning error obtained thanks to our software contains sometimes an outlier probably due to geometric effects. These outliers are very few: about 1 or 2 per day on average. Further investigation is needed to explain the real causes of these odd values. In any case, these outliers were removed from the data so that the plots presented in figures 5.1 to 5.4 are clean and representative of the ionospheric effects.

5.2. Graphical correlations

Figures 5.1 to 5.4 show the ionospheric effects on double differences and positioning respectively for the days:

- 103/07 (quiet ionospheric day);
- 359/04 (medium-amplitude TID);
- 301/03 (large-amplitude TID);
- 324/03 (severe geomagnetic storm).

Graphical scales are identical for each day and each baseline except for DOY 324/03 where the axis limits have been enlarged to plot the whole dataset.

5.2.1 Quiet day 103/07 (figure 5.1)

For the whole quiet day in terms of ionospheric disturbances, we can see that the ionospheric residual term $I_{AB,GF}^{ij}$ (plotted in black) is very close to zero for all of the analyzed baselines. The positioning error (red line) due to the ionosphere sometimes

reaches the value of 4-5 cm, particularly for the 20 km long baselines GILL-MECH, OUDE-ZWEV and OUDE-GENT. We can observe that, on average, the positioning error is quite lower for the smallest baseline than for the other ones. Let's recall that the nominal RTK accuracy level is a few centimeters. Therefore, we can consider that ionospheric effects of 4-5 cm are not “out of tolerance”, in particular for a 20 km baseline.

5.2.2 Day with medium-amplitude TID: 359/04 (figure 5.2)

From the residual term $I_{AB,GF}^{ij}$ we can observe that the ionospheric activity induced by the TID occurred mainly between 8 A.M. and 2 P.M. with a maximal variability around 10 A.M. These observations are in agreement with the ionospheric variability observed with the one-station method (see figure 5.3 in WP 220). We can also observe that the positioning error increases when $I_{AB,GF}^{ij}$ increases; this effect is observed for all baselines.

The absolute value of the ionospheric residual term $I_{AB,GF}^{ij}$ is generally lower for the smallest baseline GILL-LEEU than for the other ones. The maximal positioning error values reached for the baselines GILL-LEEU are about 9 cm while these values exceed 10-12 cm for a few cases on longer baselines. The largest positioning error has been observed for the baseline GILL-MECH and is close to 15 cm, what is significantly larger than the maximum value obtained in section 4 based on a 15 minute period only.

Let us note that this largest value of 15 cm was not due to the TID observed around noon but was due to a small structure similar to a TID which occurred during 30 minutes around 18h30. Let us also remark that this structure was not visible for all the analyzed baselines: for example, the ionospheric residual term $I_{AB,GF}^{ij}$ remains very quiet for OUDE-ZWEV while OUDE-MECH clearly detected the structure. This observation confirms the conclusions of WP 220: the baseline orientation has clearly an influence on the way that ionospheric structures are “seen” in double differences. Moreover, the positioning error due to ionosphere seems to be correlated with the term $I_{AB,GF}^{ij}$ because the peak in positioning error appears simultaneously than this small ionospheric structure for OUDE-MECH.

5.2.3 Day with large-amplitude TID: 301/03 (figure 5.3)

The analysis of figure 5.3 shows that the TID induces an increase in the ionospheric residual term $I_{AB,GF}^{ij}$ from 6-7 A.M. to approximately 2 P.M. The temporal variability of this term is smaller for the smallest baseline GILL-LEEU than for the other ones, as it is the case for the TID of DOY 359/04. This observation is in accordance with the results obtained in WP 220 (see section 5.5.2 WP 220) which conclude that the ionospheric residual term increases with increasing baseline length. Moreover, we can observe that,

as for the TID of DOY 359/04, the positioning error is also smaller for this same baseline GILL-LEEU.

The maximal positioning error is observed for the baseline OUDE-GENT at 11 A.M. However, let us remind that a powerful solar flare occurred exactly at the same time; this flare increased dramatically the TEC and the variability in TEC (RoTEC) was very large during a few minutes (see WP 220 section 4.2.2). Therefore, we have not to take this period into account to assess the effect of the large-amplitude TID which appeared earlier and disappeared later than the solar flare, which induces a very sudden ionospheric phenomenon. If we have a look at the positioning error earlier or later than 11 A.M, we can see that the maximum values are larger than the maximum values relative to the medium-amplitude TID of DOY 359/04. If we do not take the positioning error of 11 A.M. into account, the maximal positioning error during the day has been observed for the baseline GILL-MECH; its value is about 22 cm. Nevertheless, we can also conclude that the largest positioning error on a 20 km baseline due to a powerful solar flare is approximately 25 cm.

5.2.4 Day with severe geomagnetic storm: 324/03 (figure 5.4)

Figure 5.4 shows that the ionospheric effects due to the geomagnetic storm took place from noon and lasted until the end of the day. However, we can identify two very variable periods around 17h and 22h. The ionospheric residual term and the positioning error due to the ionosphere are the largest during these two time intervals.

We can also observe from figure 5.4 that the ionospheric effects (in $I_{AB,GF}^j$ term and also in the positioning error) are smaller for the smallest baseline GILL-LEEU, as for the previous disturbed days.

The daily maximum value of the positioning error due to the ionosphere has been observed for the baseline GILL-MECH and is about 80 cm.

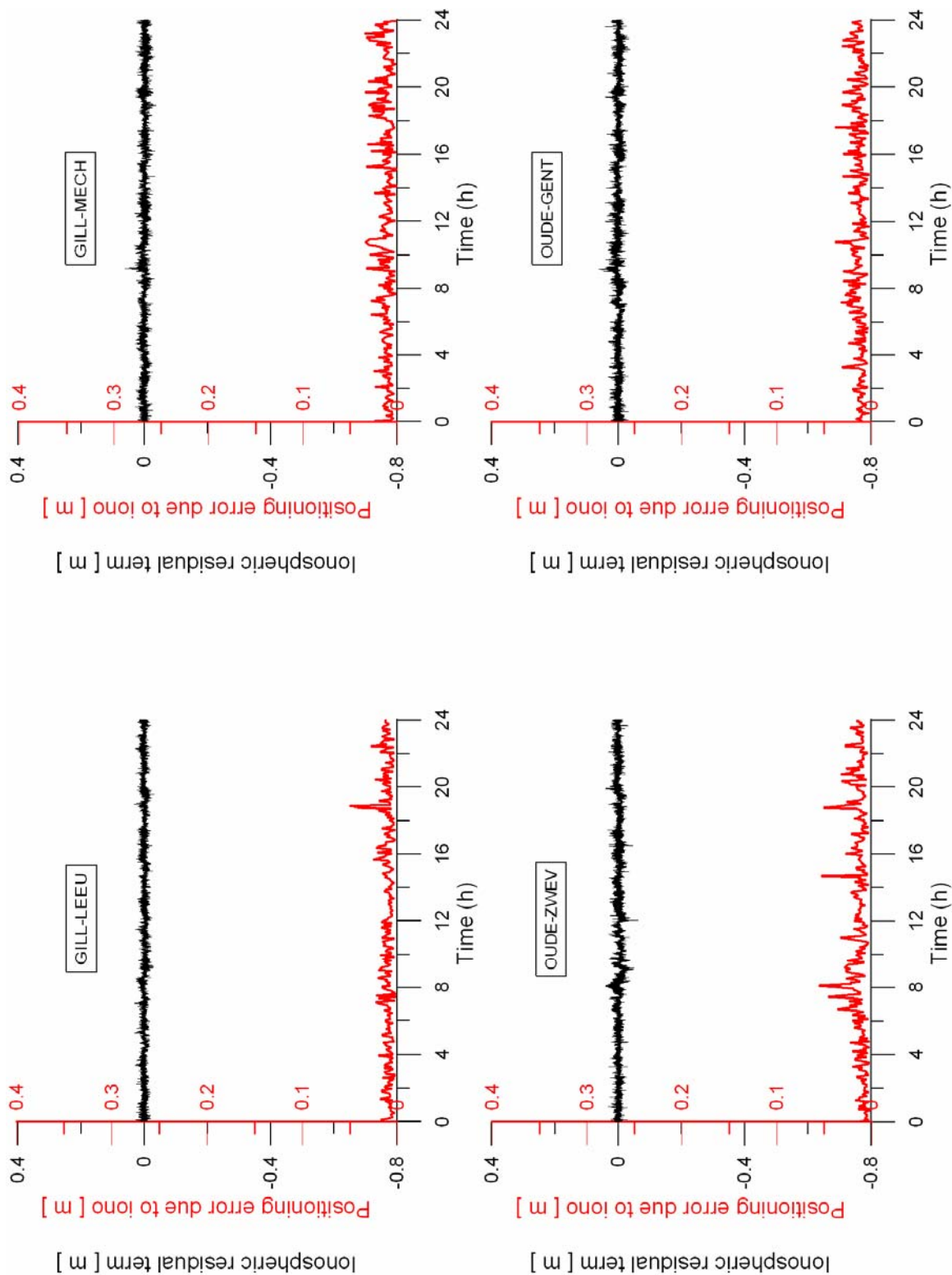


Figure 5.1. Ionospheric effects on term $I_{AB,GF}^{ij}$ (black) and on the positioning error (red) for DOY 103/07.

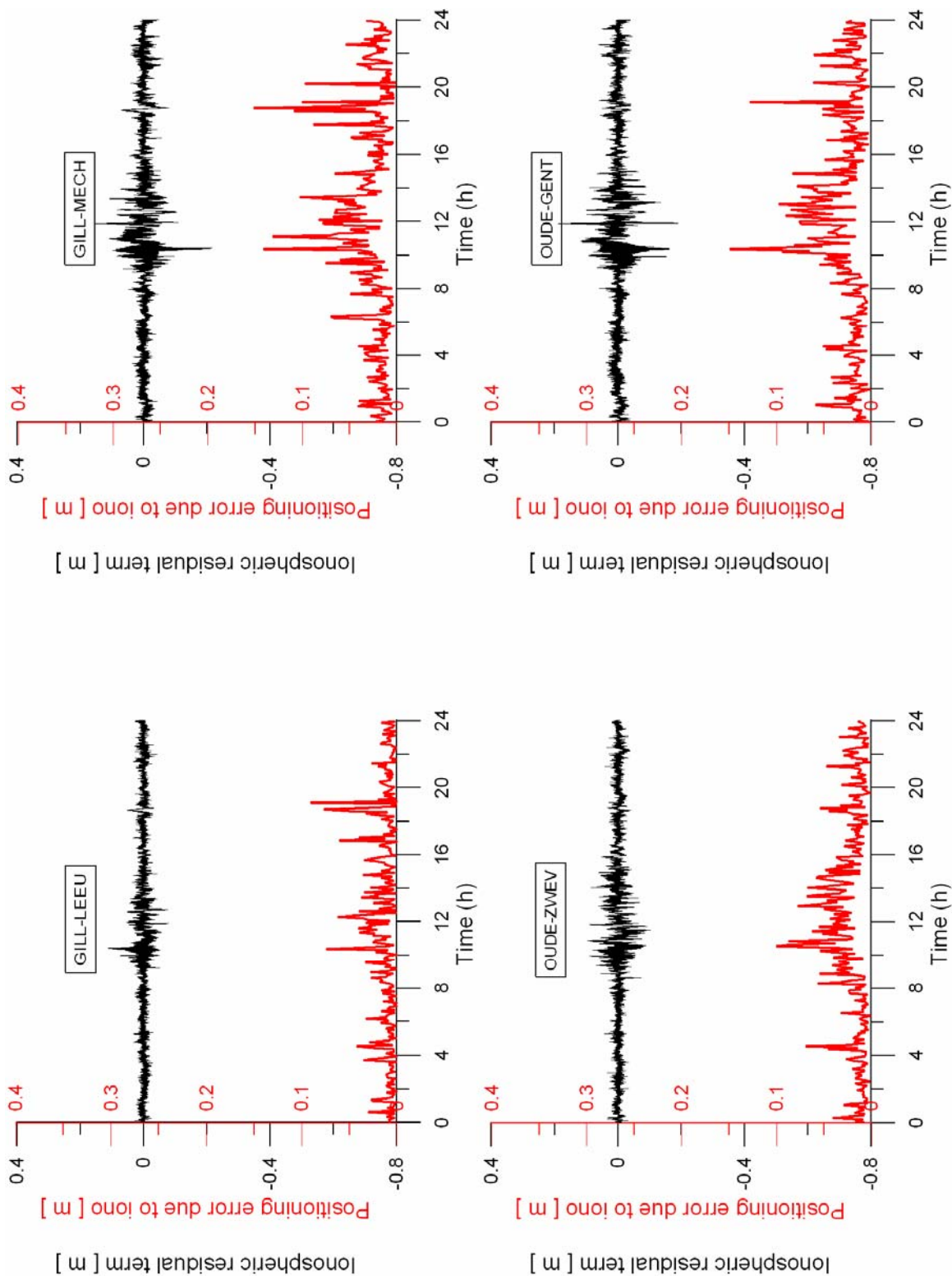


Figure 5.2. Ionospheric effects on term $I_{AB,GF}^{ij}$ (black) and on the positioning error (red) for DOY 359/04.

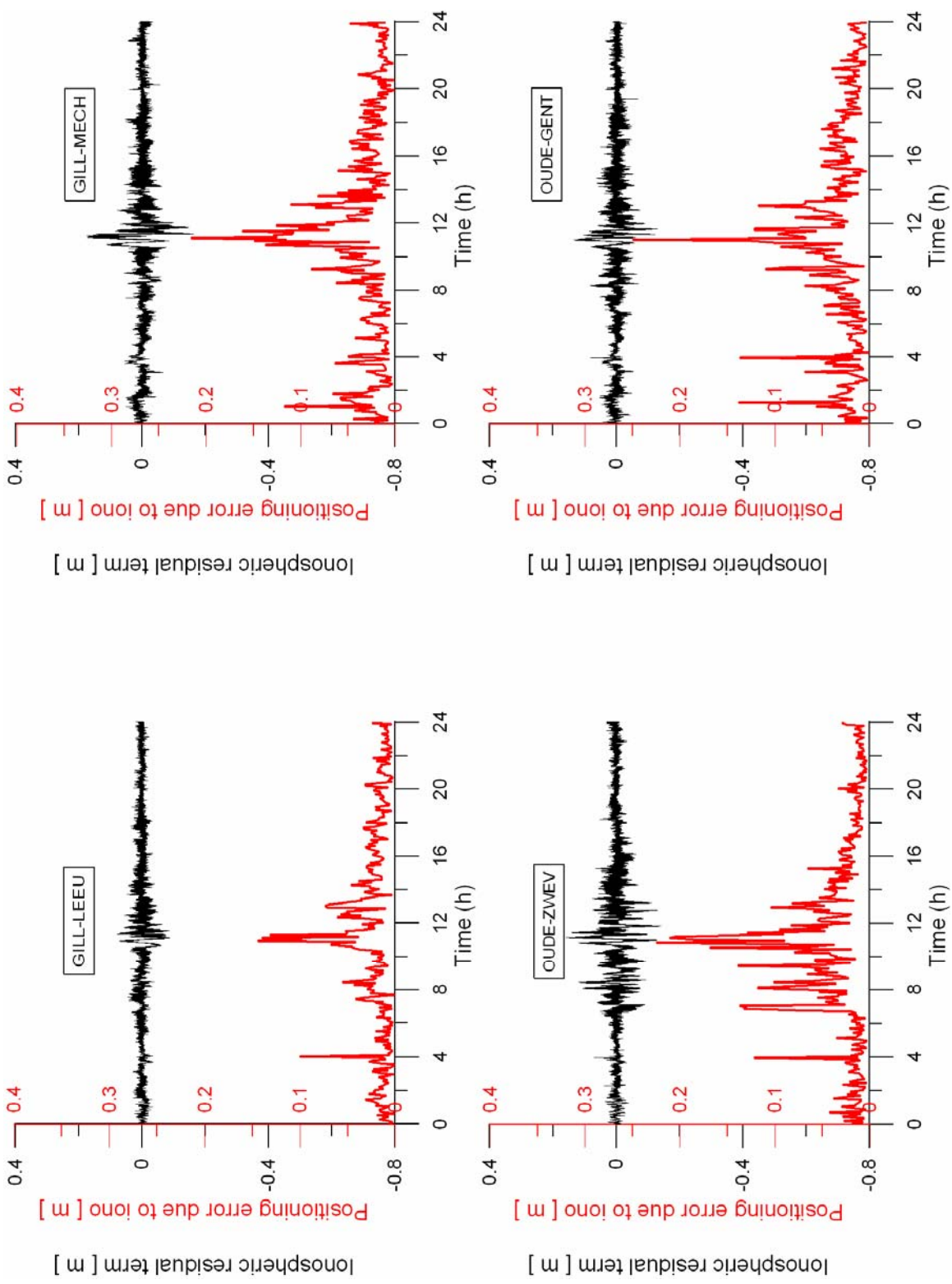


Figure 5.3. Ionospheric effects on term $I_{AB,GF}^{ij}$ (black) and on the positioning error (red) for DOY 301/03.

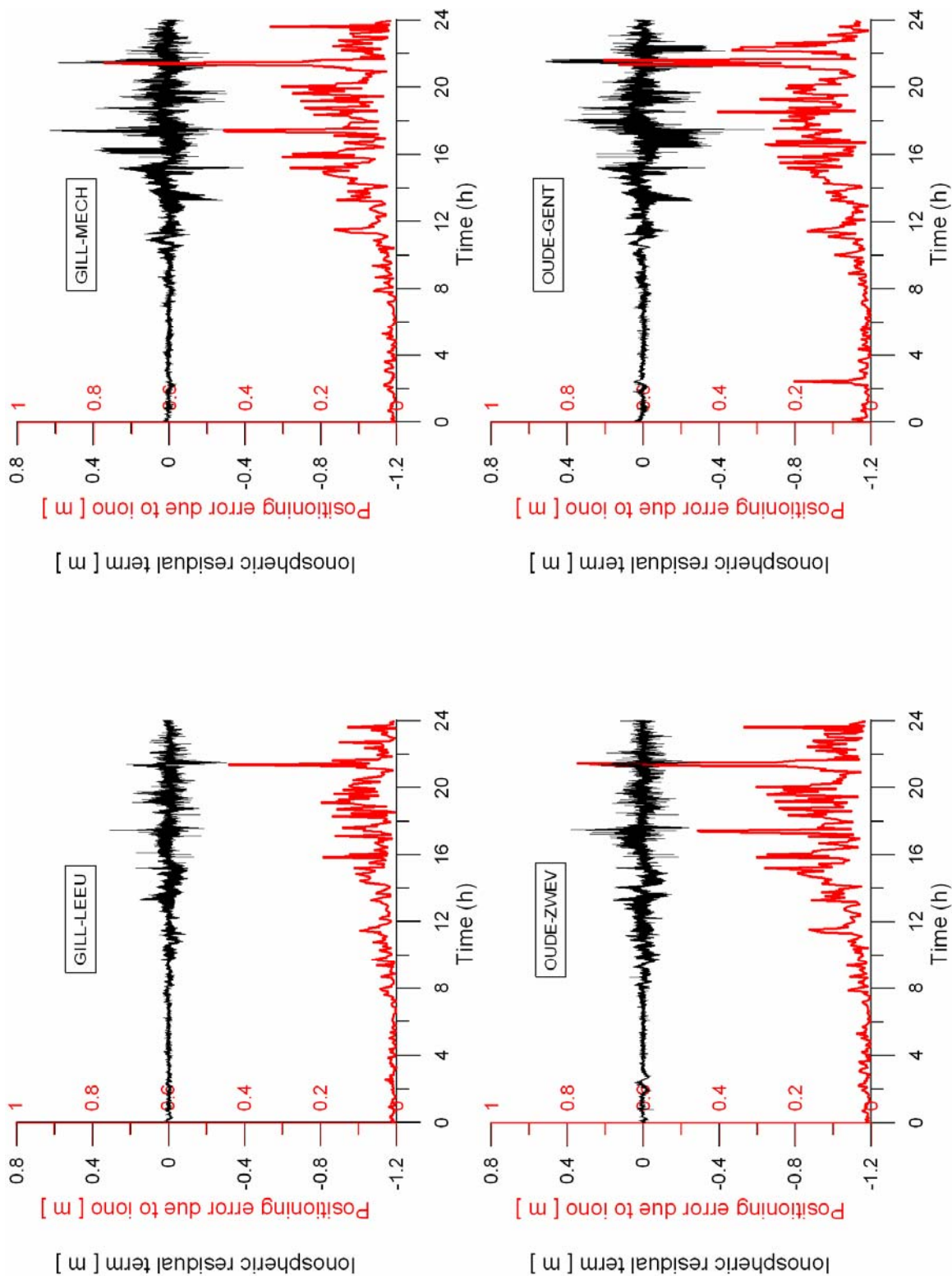


Figure 5.4. Ionospheric effects on term $I_{AB,GF}^{ij}$ (black) and on the positioning error (red) for DOY 324/03.

5.3. Positioning error and ambiguity resolution

Positioning error values obtained in sections 4 & 5 correspond to the positioning error only due to the ionosphere and are representative only for RTK users who have already fixed their ambiguities to the correct integer values. Indeed, in our study, the ambiguities are solved using our own software which takes into account the whole visibility period of the different satellite pairs; the ionospheric effects are assessed afterwards. Therefore, this method is not representative of the error which will be experienced by a user during the so-called “initialization phase” where he has to wait that ambiguities are solved to the correct integer before starting surveying. In practice, positioning error obtained during the occurrence of ionospheric disturbances can reach values which are much larger than values obtained in sections 4 & 5 because such structures can affect the real-time ambiguity resolution process implemented in the user’s receiver. Indeed, if during the ambiguity resolution process, the ionospheric residual term is equal to or is larger than half a GPS-cycle, the ambiguities might be fixed to wrong integer values, which can lead to very large positioning errors. This effect has not been taken into account in our study.

However, we implemented a method allowing a real-time ambiguity resolution process based on float ambiguities and their covariance matrix as input: the so-called “LAMBDA” method (Joosten & Tiberius, 2000). In order to illustrate the positioning error that a user can experience on the field in case of ionospheric disturbances, we chose to plot the positioning error during the occurrence of the medium-amplitude TID of DOY 359/04. As for our previous results, the positioning error is computed within 5 minute time intervals.

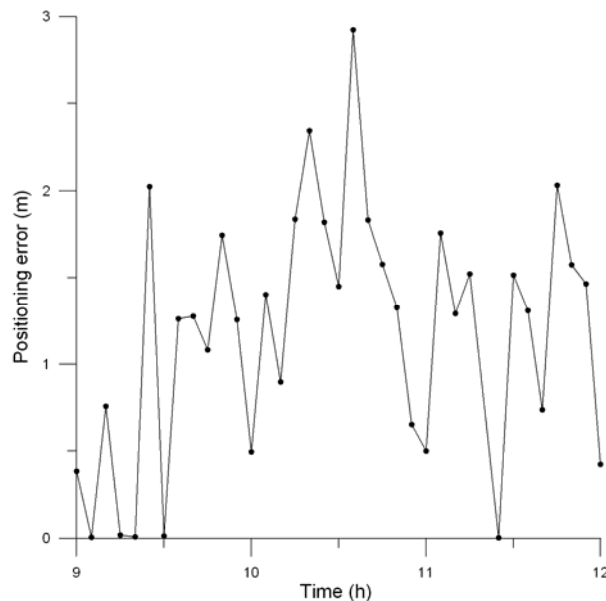


Figure 5.5. Positioning error for DOY 359/04 on baseline GILL-LEEU (11.3 km) when considering the LAMBDA ambiguity resolution technique.

The analysis of figure 5.5 shows that positioning error values exceed 1 m and can reach nearly 3 m for a baseline of only 11 km. When comparing these values with the values discussed in section 5.2.2, we can observe that the errors obtained with the real-time method are more than ten times larger than the values obtained if the ambiguities are correctly solved. In fact, if ambiguity resolution gives wrong integer values during the initialization phase, the user position will be affected by these wrong ambiguities during the whole surveying period. However, although the positioning errors obtained with the real-time method correspond to the real situation encountered on the field, they do not reflect the direct effects of the ionosphere on positioning when the ambiguities have been successfully solved. In reality, it is not very useful to assess ionospheric error during initialization phase: the magnitude of the error experienced during initialization is not an important parameter. It is much more realistic to assess the ionospheric error after ambiguity resolution: it allows to warn users when the level of ionospheric error reaches half a cycle, what will clearly be the origin of strong degradations for users who are trying to solve their ambiguities.

6 QUANTITATIVE STUDY OF THE POSITIONING ERROR DUE TO THE NEUTRAL ATMOSPHERE

In WP 250, we have developed an index which allows to detect the presence of small-scale structures in the neutral atmosphere. In this section, we use the technique outlined in section 3 to assess the influence of such structures on RTK positioning: we compute the absolute value of the difference between the “true” station position and the computed position $(X_{B,2}, Y_{B,2}, Z_{B,2})$ which is obtained based on double differences corrected for differential ionospheric effects. It is important to underline that this strategy has a disadvantage: not only small-scale structures in the neutral atmosphere can be the origin of large differences between these positions; indeed, other error sources still affect the computed position $(X_{B,2}, Y_{B,2}, Z_{B,2})$:

- Residual multipath and measurement noise;
- Bad satellite coverage (bad geometry);
- Tropospheric “thickness”: it is important to recall that our tropospheric index has been developed in order to detect irregular structures; it is computed based on double differences of the ionospheric-free combination. In practice, to isolate the effects of small-scale structures on this combination, we fit it using a 3rd order polynomial and we compute residuals to the fit. This procedure removes elevation effects (see WP 250 figure 15 p. 26), i.e. tropospheric differential effects due to satellites at low elevations. These effects which usually remain negligible for short baselines (< 10 km) can become larger for baselines of about 20 km. It is also important to recall that the goal of our project is to detect phenomena which could pose a threat for high accuracy real time positioning; therefore, “elevation effects” are outside of the scope of our study.

From equation 2.10 in WP 250, it can be seen that positions computed using ionospheric-free combination are affected by the same error sources as the positions computed by the method outlined in section 3. In addition, the measurement noise of the ionospheric-free combination is larger. This is the reason why we did not use the ionospheric-free combination to assess the positioning error due to small-scale structures in the neutral atmosphere.

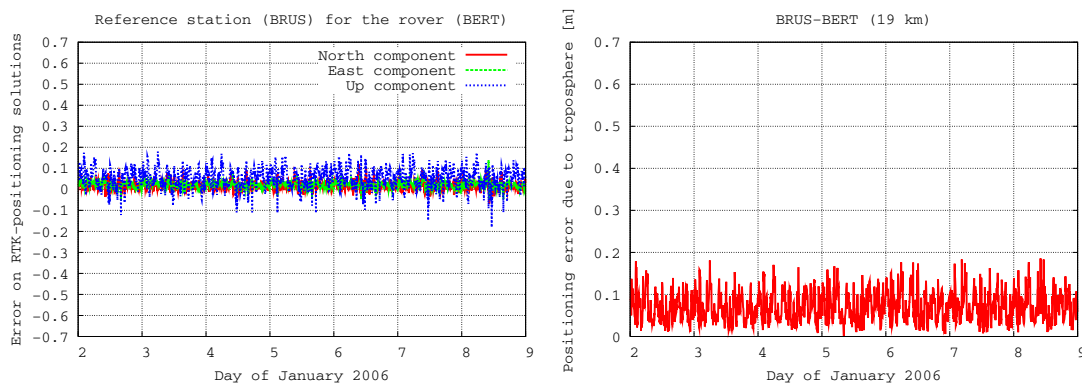


Figure 6.1 Error on RTK positions for north, east and up components (on the left) of baseline BRUS-BERT; positioning error expressed in distance is shown on the right. Positioning errors are shown from 02/01/2006 to 09/01/2006.

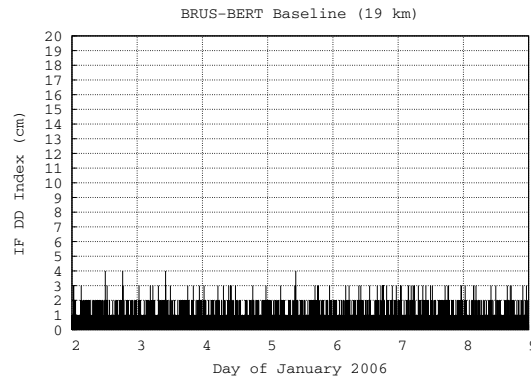


Figure 6.2 IF DD Index for baseline BRUS-BERT from 02/01/2006 to 09/01/2006.

To be able to “extract” the contribution of small-scale tropospheric structures to the positioning error obtained from the method outlined in section 3, it is important to assess the positioning error experienced during quiet tropospheric conditions (as measured by our tropospheric index).

In figure 6.1 we present the error on RTK positions for the three components of BERT station (rover) considering BRUS as reference station from 02/01/2006 to 09/01/2006. The error on the three components of the position can also be expressed in terms of distances according to equation (5.1). The 7 days selected in January 2006 present small IF DD Index (see table 1 of WP 250 and figure 6.2). Despite the fact that no IF DD Index larger than 4 is observed during these days, we can see that for a baseline of about 20 km, the positioning error (distance) due to all error sources (except ionosphere and small-scale structures in troposphere) ranges from a few centimetres up to about 18 cm. This level of error can be explained by the fact that 20 km is considered as the maximum acceptable baseline length for usual RTK applications.

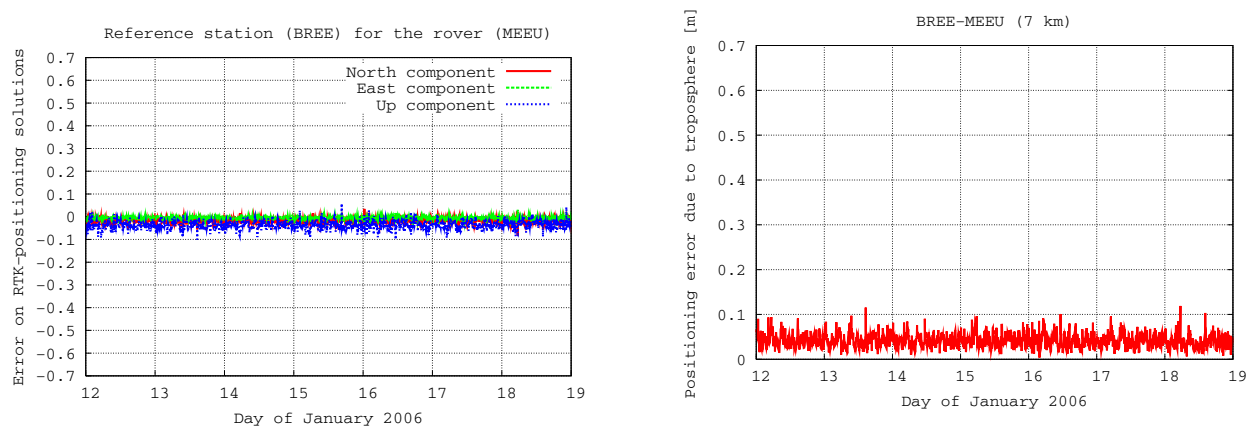


Figure 6.3 Error on RTK positions for north, east and up components (left) and on distance for baseline BREE-MEEU from the 12/01/2006 to 19/01/2006.

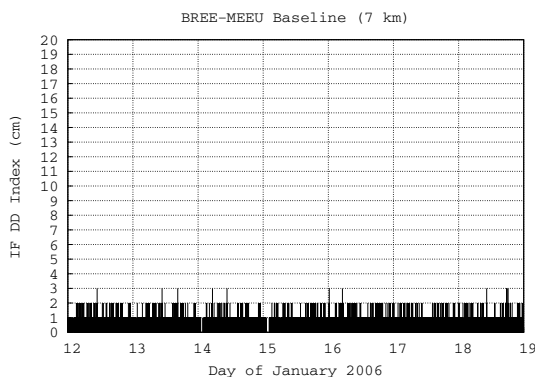


Figure 6.4 IF DD Index of baseline BREE-MEEU from the 12/01/2006 to 19/01/2006.

We performed the same test for baseline BREE-MEEU (7km) from 12/01/2006 to 19/01/2006; IF DD Index is smaller or equal to 3 during the whole considered period what represents quiet tropospheric conditions (figure 6.4). Figure 6.3 shows that the positioning error remains smaller than 10 cm except in a few cases (4 cases on 7 days). From this point, we can conclude that it will be much easier to “extract” the contribution of small-scale tropospheric structures to the positioning error by analyzing shorter baselines.

In practice, we processed the days with the largest IF DD Index values for the baselines which have been studied in WP 250: BRUS-BERT, BRUS-OLLN, BREE-MEEU. We present here the main conclusions from this study:

1) In most of studied cases, IF DD Indexes larger or equal to 5 (the so-called “5+” category in WP 250) are the origin of degradations in positioning errors which range between 20 cm and 40 cm even on short baselines (35 cm on BREE-MEEU (7 km) and 31 cm on BRUS-GILL (4 km)).

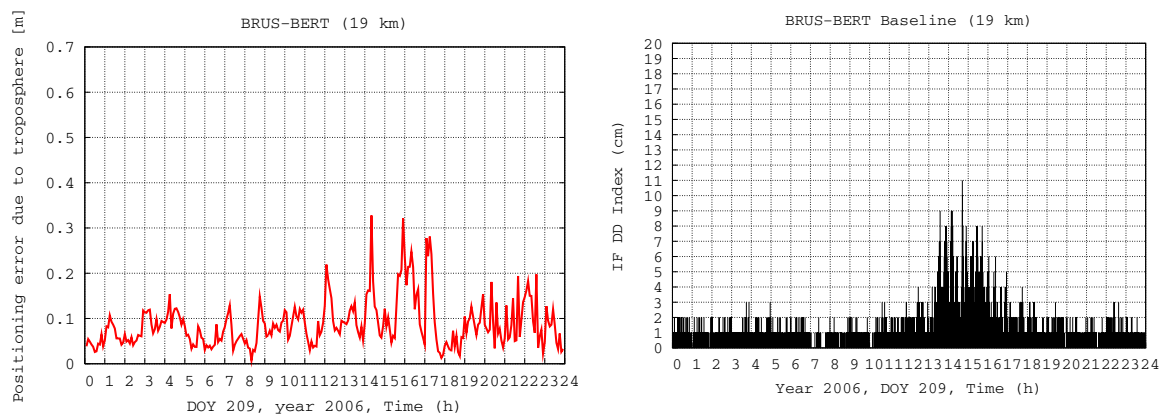


Figure 6.5 Errors on distance (left) and IF DD Index (right) for baseline BRUS-BERT on 28/07/2006.

Figure 6.5 shows IF DD index and errors on distance for baseline BRUS-BERT observed on 28/07/2006 when heavy rainfalls have been observed (see WP 250 for more details). Even if the “background” positioning error on baseline BRUS-BERT ranges from 5 cm to 20 cm, the occurrence of IF DD Indexes of 5+ category is the origin of increased positioning errors of more than 30 cm.

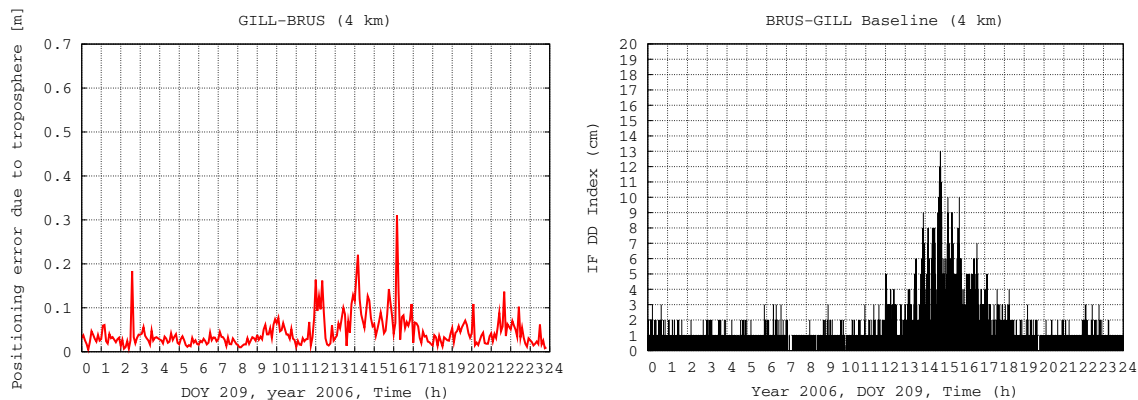


Figure 6.6 Errors on distance (left) and IF DD Index (right) for baseline BRUS-GILL on 28/07/2006.

Figure 6.6 shows IF DD Index and errors on distance for baseline BRUS-GILL (4 km) observed on 28/07/2006. IF DD Indexes of 5+ category are observed from 12h00 to 17h00, which corresponds to positioning errors up to 30 cm, even on such a short baseline. It is clear that in the case of short baselines, it is easier to “extract” the contribution of small-scale tropospheric structures from the background positioning error.

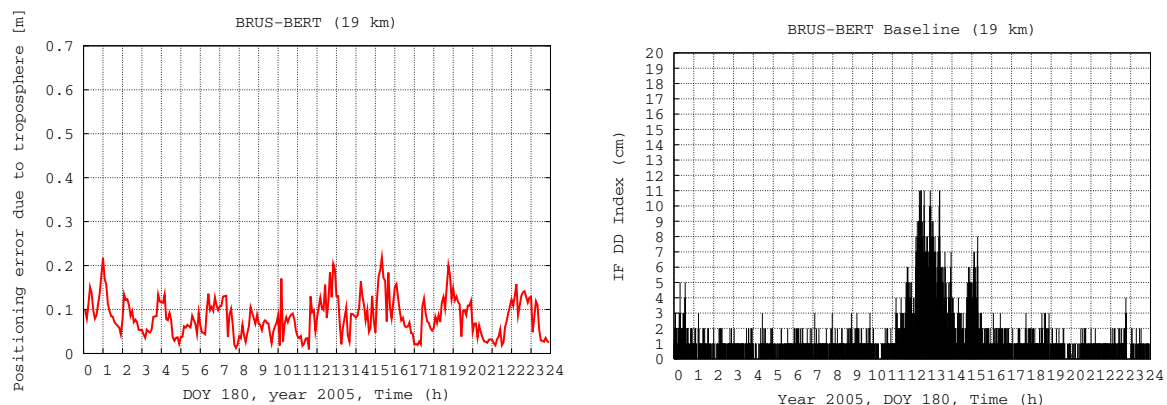


Figure 6.7 Errors on distance (left) and IF DD Index (right) for baseline BRUS-BERT on 29/05/2005.

Figure 6.7 shows IF DD index and errors on distance for baseline BRUS-BERT (19 km) observed on 29/05/2005. This event has also been studied in details in WP 250. IF DD Indexes of 5+ category are observed from 00h00 to 01h00 and from about 11h30 to

15h30. In this case, the error due to small-scale tropospheric structures cannot be extracted from the background error.

2) There is no “linear” relationship between the magnitude of the IF DD Index and the magnitude of the positioning error. This fact can be understood rather easily: as already explained, the station position is computed based on a least square adjustment of all available satellite pairs for the considered period. On the one hand, the number of satellite pairs which are affected by the structures has an important influence on the positioning error: for example, conditions where 5 satellite pairs are affected by an index of 5 could be the origin of larger errors than conditions where only one satellite is affected by a large index of 15. On the other hand, from the theory of error propagation, we know that an increased uncertainty on the measured quantities (double differences) results in an increased uncertainty in the derived parameters (positions): this means that a larger error in the double differences gives a higher probability to have a larger error in the computed position but this position will not necessarily be larger in the reality.

This is illustrated by figure 6.8 which shows IF DD Index and errors on distance for baseline BREE-MEEU observed on 06/06/1998: between 07h00 and 8h00, an index of 6 is observed while the positioning error is close to 30 cm; around 17h00, an index of 13 is observed while the positioning error is close to 10 cm (rather close to the background error).

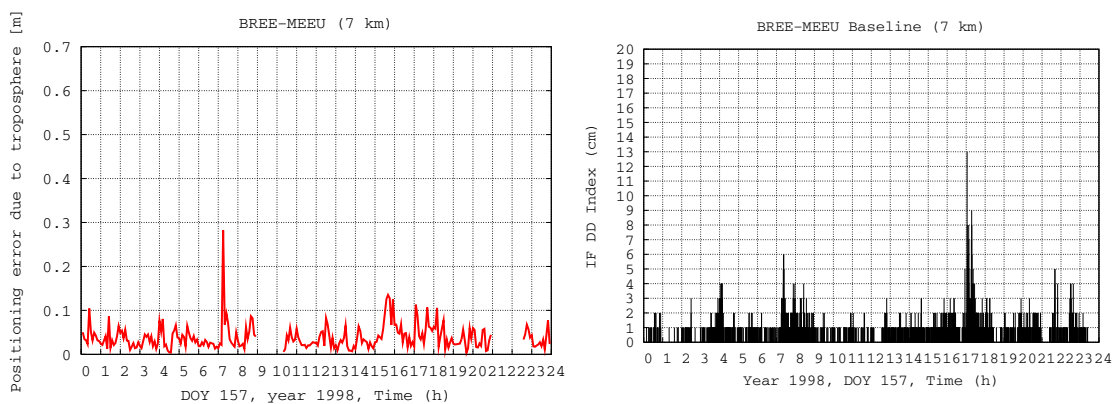


Figure 6.8 Errors on distance (left) and IF DD Index (right) for baseline BREE-MEEU on 06/06/1998.

3) We sometimes observe still unexplained peaks in the positioning error time series. Some of them are larger than one meter and have been considered as outliers: they are probably related to unfixed problems in our software. In other cases, we observe smaller peaks (see for example the peak in figure 6.6 between 2h00 and 3h00 which does not correspond to a period with large IF DD Index). It could be due to other problems like bad geometry, for example. Further investigations are necessary to understand the origin of these peaks.

7 IONOSPHERIC EFFECTS ON AVIATION

Applications in aviation are based on carrier-smoothed code observables. Aircrafts use differential corrections provided by reference stations in order to improve the accuracy of their computed positions.

For a given satellite i , the code measurement made by the user (aircraft) is affected by an ionospheric error I_u^i (also called slant ionospheric delay) given by (equation 2.2):

$$I_u^i = 40.3 \frac{TEC_u^i}{f^2} \quad (7.1)$$

At the same time, the code measurement made by the reference station on the same satellite i is affected by an ionospheric error I_r^i given by:

$$I_r^i = 40.3 \frac{TEC_r^i}{f^2} \quad (7.2)$$

The reference station provides I_r^i as ionospheric correction to the user. Therefore, the quality of the differential ionospheric correction will depend on the difference $I_u^i - I_r^i$ (the difference in slant delays experienced by the user and by the reference station). This difference depends on $TEC_u^i - TEC_r^i$ (equations (7.1) and (7.2)). Small-scale structures in the ionosphere can be the origin of differences in slant delays which can pose a threat for applications in aviation.

Ionospheric storms can have significant adverse effects on the performance of present-day technological systems, including satellite navigation for aviation. Although the satellite-based navigation for aviation purposes possesses large capabilities and advantages above conventional navigation aids, the ionospheric effects in various applications/services are still poorly investigated /understood. The observation of ionospheric effects and their interpretation are complicated by the fact that the ionosphere dynamics and the ionospheric disturbances in particular are characterized by strong variations in the vertical and horizontal electron density distribution that depend also on season and local time.

The use of satellite navigation for precision vertical guidance requires precise correction and bounding of ionospheric delay estimation errors. WAAS (Wide Area Augmentation System) has already experienced major geomagnetic storms where vertical guidance has been automatically disabled for periods lasting several hours over most of the United States (*Luo et al.*, 2003). The LAAS (Local Area Augmentation System) system assumption of a constant ionosphere variation in the area of the airport and detection of noncompliant conditions has been put under investigation since it is of high priority to the LAAS program. For the purpose, researchers have already observed and attempted to quantify the irregularity of the ionosphere during strong geomagnetic storms over CONUS in the last few years. Observations of significant ionospheric anomalies, including gradients, ‘depletion/irregularity walls’, and similar fast moving ionospheric features in the American sector have been reported for the major ionospheric storms on 6

April 2000, 29 October 2003, and 20 November 2003. For example, initial research into the rapid changes in delay during the geomagnetic storm of April 6th, 2000 identified the possibility that the delay changes were due either to very steep gradients of narrow “walls” (i.e. 20 km wide) moving slowly (100 m/s) or that these were somewhat wider walls (80—100 km) moving much more rapidly (~500 m/s) (Luo *et al.*, 2003; Dehel *et al.*, 2004). Closely spaced CORS observations of ionospheric delay changes are shown in Fig.7-1.

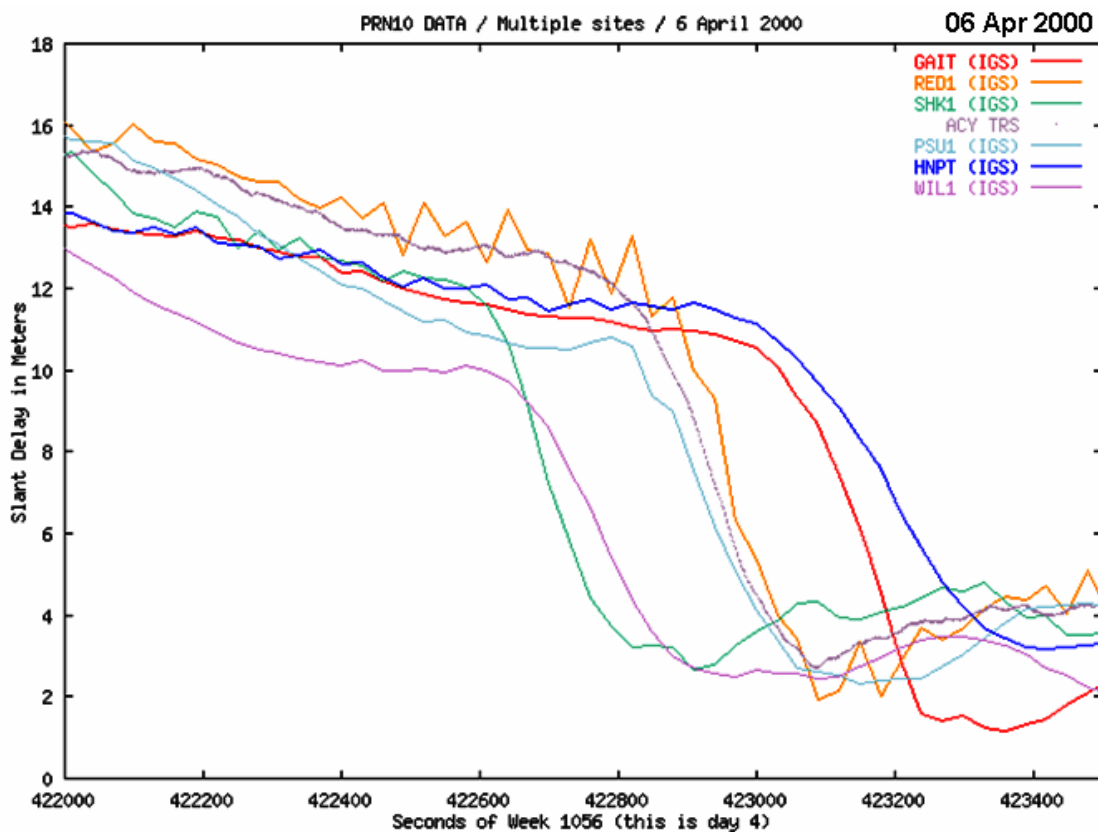


Fig.7-1. Ionospheric delay drop during the geomagnetic storm on 6 April 2000 at multiple sites in the Washington D.C. area showing the ‘wall’ motion.

Observations of these ionospheric features remain limited and the underlying physics is still not well understood. Therefore, it will be interesting to learn if such features were observed in other longitudes during these or other strong geomagnetic storms, since the international GBAS (Ground Based Augmentation System) and SBAS (Space Based Augmentation System) systems will need to be provably-safe during geomagnetic storms (Dehel *et al.*, 2004).

The research reported in this section addresses the issue of the ionospheric ‘irregularity walls’ and associated phenomena. Presented are our observations and research based on analyses of the local TEC / slant delay behaviour. Comparisons are made with the corresponding American observations during the storms of 29 October 2003 and 20 November 2003.

7.1 Case studies of ionospheric gradient anomalies

For the purpose of studying ionospheric gradient anomalies, we have selected several GPS stations in Belgium (Fig.7-2), namely BRUS (50°47'N, 04°21'E), DENT (50°56'N, 03°23'E), BREE (51°08'N, 05°38'E), WARE (50°41'N, 05°14'E), and DOUR (50°05'N, 04°35'E). Each station is assigned a unique colour code which will be used when plotting the measurements made at this station. The above-mentioned stations were selected because of their geographic locations, optimal distance from one another and alignment, suitable for detection of the ionospheric disturbances/anomalies we are focused on in this report.

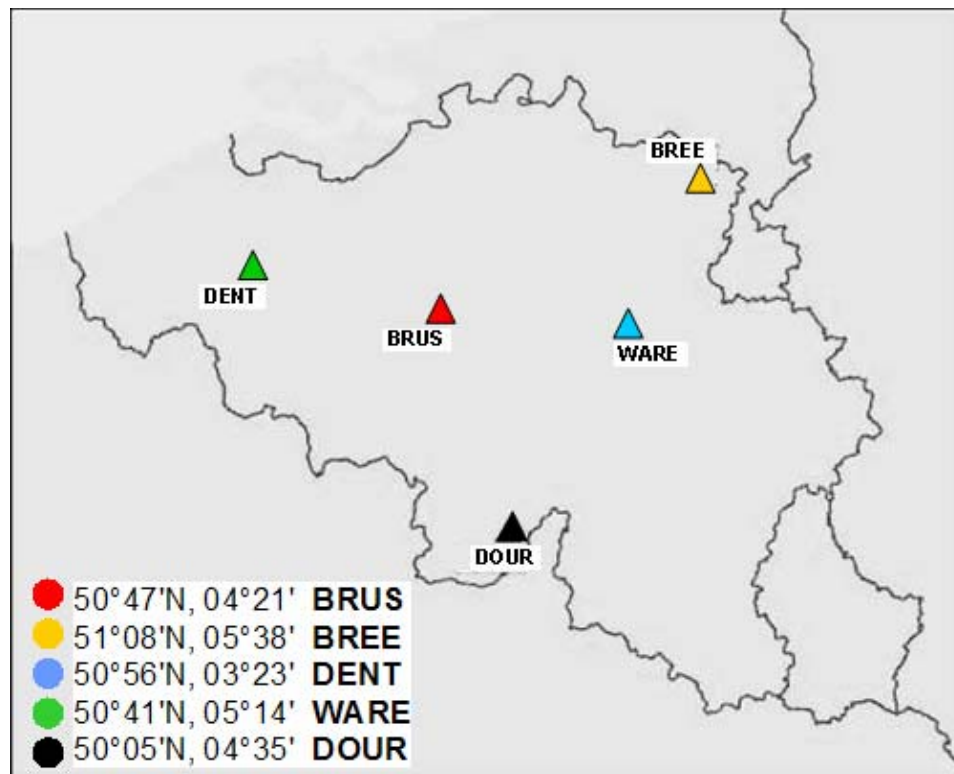


Fig.7-2. Map of Belgium with the GPS stations used for this study.

Although data from all GPS stations was used, mostly results from the BREE-WARE-DOUR set of stations will be presented here. One important reason for such selection is the typical propagation patterns of ionospheric disturbances during storms. To demonstrate the propagation, the TEC relative deviation from median, $DTEC = (TEC - TEC_{med}) / TEC_{med}$, is used. The ratio enhances the perturbation effects and facilitates the interpretation. For example, the observed increase of relative TEC between 0600 and 1400 UT during the storm on 24 July 2004 appears first at northern high latitudes and then propagates steadily in SW direction (Fig.7-3). The development and propagation of such an increase is explained with the action of an eastward directed electric field which penetrates from high latitudes toward lower latitudes and thus lifts up the plasma via the electromagnetic ($E \times B$) drift effect, resulting in a reduced loss rate, that is, in a positive DTEC response.

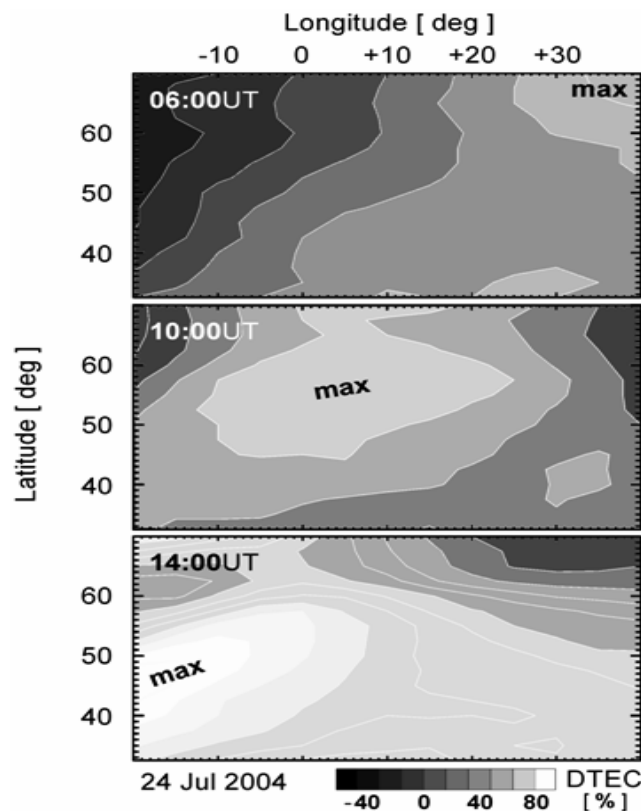


Fig.7-3. Relative TEC observed during the storm on 24 July 2004 (*Stankov et al., 2006*).

In fact, the ‘irregularity walls’, detected in the American sector during the storms of 6 April 2000, 29 October 2003, and 20 November 2003, all follow a similar propagation pattern.

7.1.1 The ionospheric storm on 29 October 2003

During the whole month of October 2003 the geomagnetic activity was low except during the last 3 days when a large storm took place. The events at the end of October 2003 were characterized by a series of large radiation bursts at the Sun and huge coronal mass ejections (CMEs) causing severe perturbations in the geomagnetic field and in the geoplasm environment formed by the magneto- and ionosphere. On 28 October, while the sunspot group 486 faced directly toward Earth, a huge solar flare was observed which was the third largest on record since 1976. The corresponding CME left the sun at about 2000 km/s reaching the Earth magnetosphere already after 19 hours, around 06:00UT on 29th October. The subsequent geomagnetic storm was one of the largest in the past 40 years continuing well into 30th and 31st of October. For most of the time on 29 October the recorded planetary geomagnetic index Kp was close to its maximum possible value of 9, indicating severe geomagnetic and ionospheric conditions (**Fig.7-4**). Similarly, the other geomagnetic index, Dst, strongly related to the magnetospheric parameters, reached values of about -400nT, thus confirming the extreme intensity and duration of the magnetic storm. These conditions set the background for observing and experiencing strong ionospheric effects.

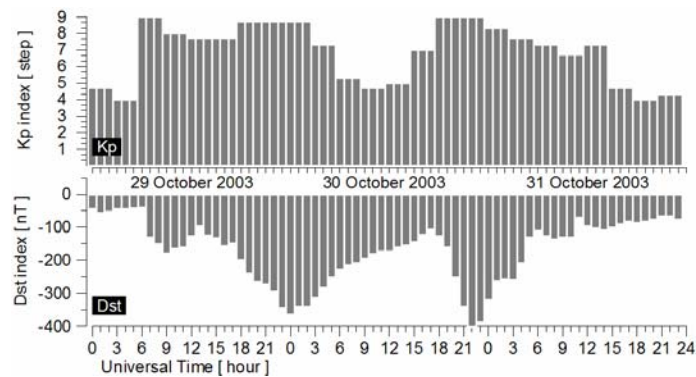


Fig.7-4. The 29-31 October 2003 ionospheric storm background as represented by the planetary geomagnetic indices Kp (top panel) and Dst (bottom panel)..

During the storm period of 29-31 October 2003, reported were several significant malfunctions due to the adverse effects of the ionosphere perturbations such as interruption of the WAAS service and degradation of mid-latitudes GPS reference services. Analyses of this storm also revealed steep “walls of depletion” (Fig.7-5) moving through with high speeds and gradients of hundreds of mm/km (*Dehel et al., 2004*).

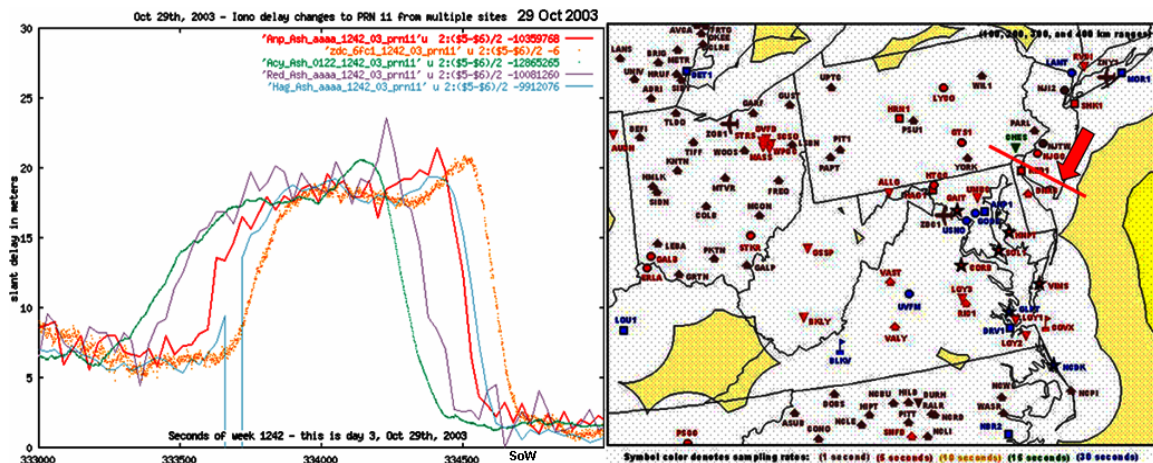


Fig.7-5. Large ionospheric delay gradients (‘walls’) (left panel) observed among CORS clusters in the Washington D.C. area (right panel) on 29 October 2003.

As already stated, it will be interesting to see if similar anomalies are observed here in Europe. For the purpose, we have analysed all available observations carried out at the selected network of GPS stations in Belgium during this particular ionospheric storm. The ionospheric delay measurements from 29 October 2003 deduced from all satellite links are plotted in the upper panel of Fig.7-6 with references to the corresponding ionospheric piercing points (IPP) given in the bottom panel. The figure clearly shows the sharp increase of the ionospheric delay during the main phase of the storm in the morning hours. This increase is sustained well into the afternoon hours in accordance to the extreme geomagnetic activity conditions (cf. Fig.7-4). It is followed by a significant drop of the delay values in the period between 1700 and 2000 UT. Hence, it is more likely to observe ‘depletion wall’ in this time period.

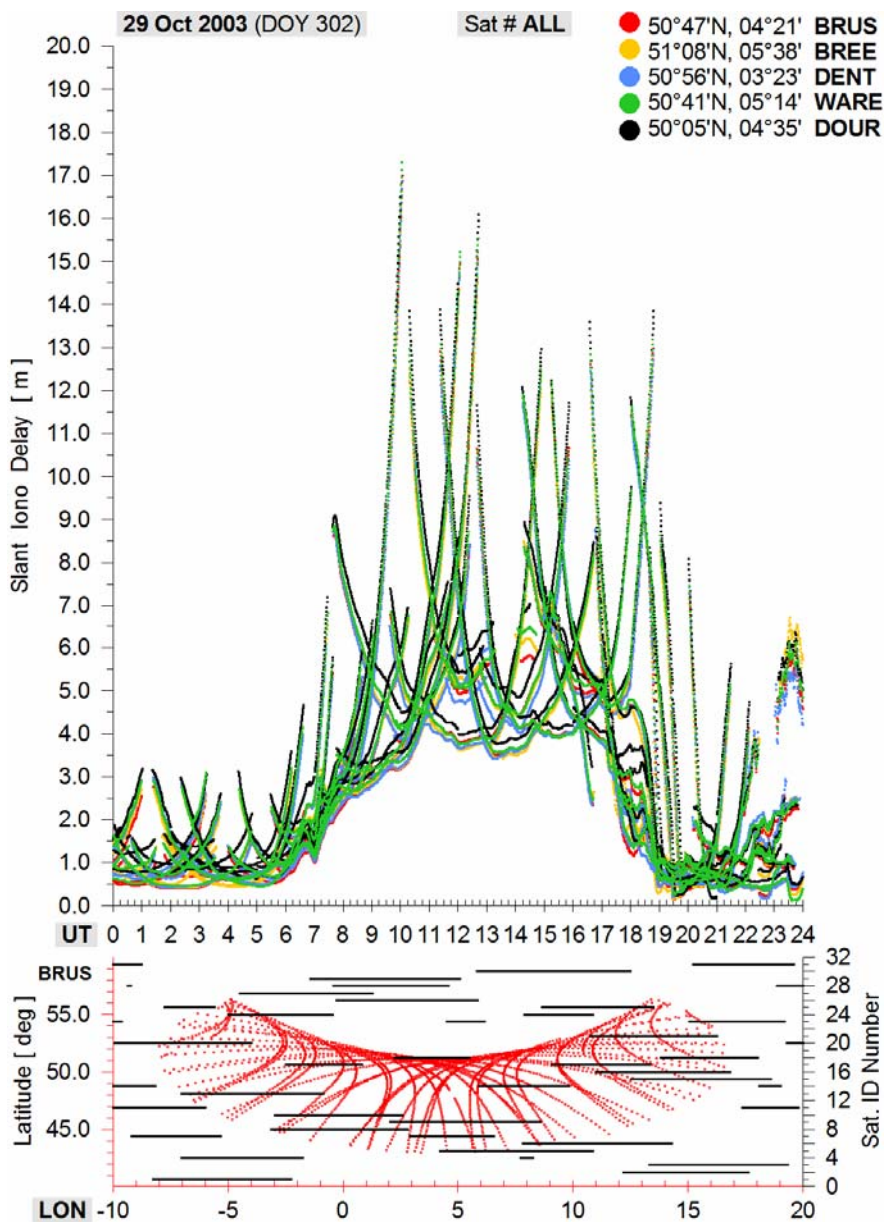


Fig.7-6. Ionospheric delays during the storm on 29 October 2003 measured via the GPS satellites ‘visible’ from the selected GPS stations in Belgium (top panel). The satellite IPP traces over Europe (with reference to the base reference station BRUS) are plotted in the bottom panel with red colour. The period of ‘visibility’ of each GPS satellite, again with reference to the BRUS station and according to UT, is plotted in the bottom panel with black solid lines.

The figure also suggests that a proper detection and analysis of ‘depletion walls’ will have to deal with various inconveniences, such as the irregular coverage of the satellite IPP traces, different shape and orientation of these traces, short-term visibility of GPS satellites, etc.

The majority of the slant ionospheric delay profiles obtained from a satellite link appear in the U-type shapes (Fig.7-7, left panel). The increases in both ends can be explained with the effect of gradually decreasing satellite elevation angle (hence increasing slant delay) combined most probably with latitudinal and/or zonal gradients in the ionospheric density. Such combination of conditions seriously impedes the analysis. In the case presented in the left panel of Fig.7-7 (Sat #5), the IPP traces have relatively small latitudinal resolution and large longitudinal coverage. As a result, what we see is a negligible latitudinal gradient except in the middle of the time period, i.e. between 13 and 15UT when the IPPs positions are close to the GPS stations. Obviously, a gradual decrease of the electron density occurs in latitude direction, with higher values at the southern station DOUR and lower values in the northern stations WARE and BREE. Longitudinal gradient seems to also take place with higher densities observed in the West. Another frequently observed situation is presented in the right-hand panel of Fig.7-7 (Sat #16) when one part of the IPP trace has East-West orientation and the other one has North-South orientation. Thus, the former part enhances possible latitudinal gradient and latter part enhances the longitudinal. Again, the IPP trace section that is nearest to the GPS stations shows undoubtedly the largest delay differences between the observations from the different stations.

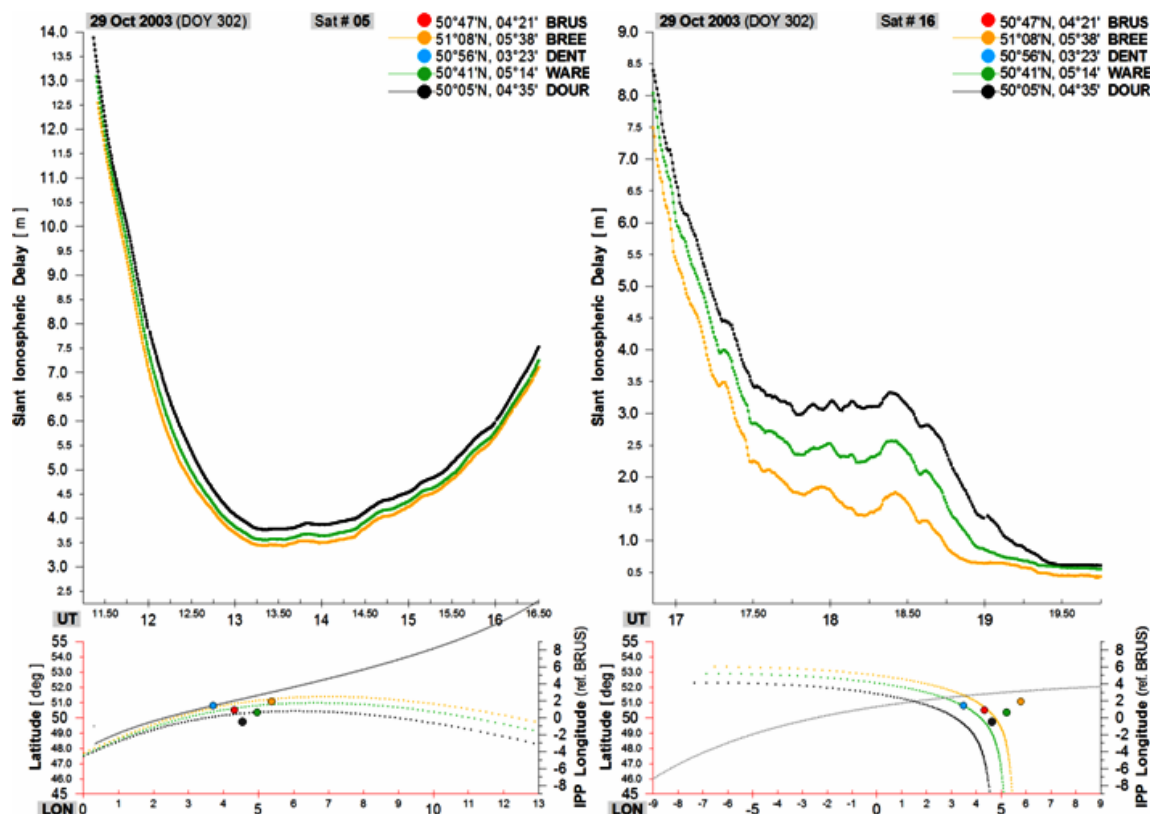


Fig.7-7. Ionospheric delays during the storm of 29 October 2003 as measured via GPS satellites No.5 (left panel) and No.16 (right panel). The bottom panels show the satellite IPP traces (colour corresponding to station) on a geographic longitude vs. latitude map. The longitudinal excursion of the satellite IPP (reference station BRUS) during the selected UT period is plotted with solid line (grey colour).

Taking into account the above-presented concerns about the IPP trace location, shape, and orientation, hundreds of slant ionospheric delay profiles have been analysed for this storm day. As expected, only a couple of profiles emerged from the period of interest, between 1700 and 2000 UT, that suggest the occurrence of moving ‘depletion walls’ (Fig.7-8).

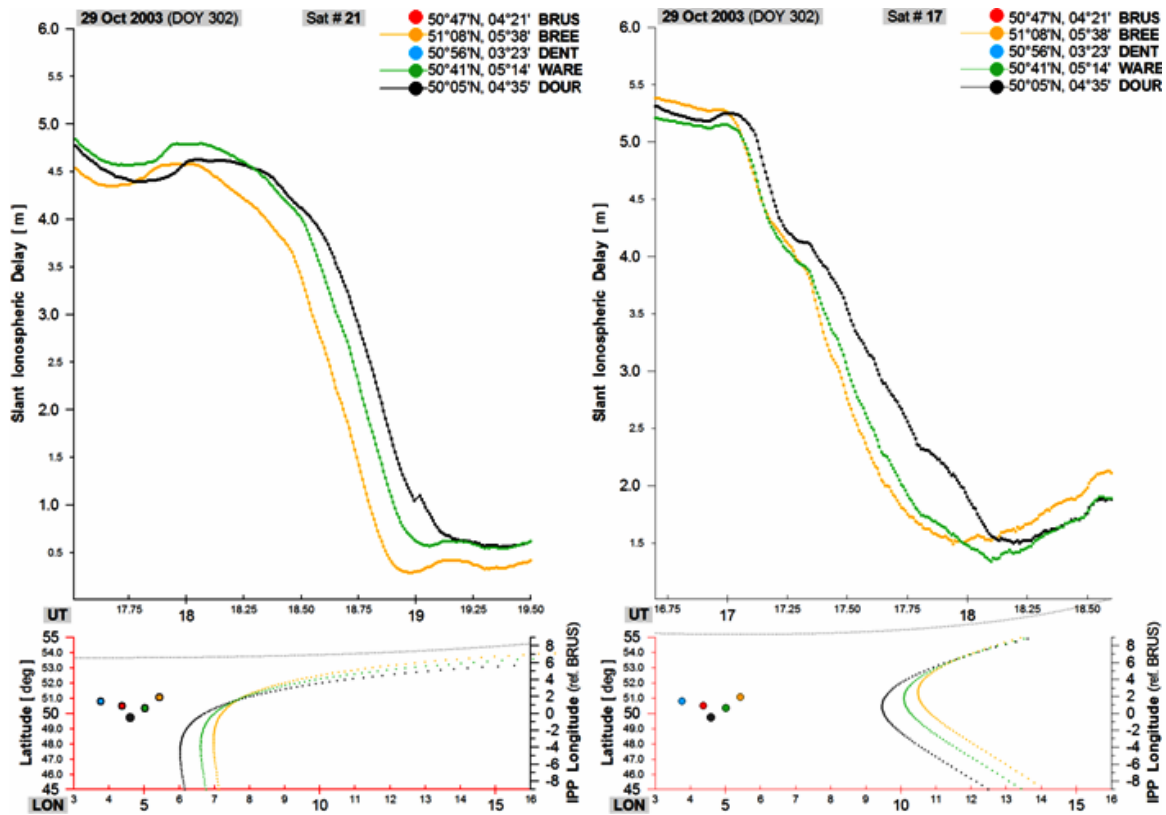


Fig.7-8. Ionospheric delay drops (‘depletion walls’) during the storm of 29 October 2003 as measured via GPS satellites No.21 (left) and No.17 (right) over Europe.

The figure shows ionospheric delay drops suggesting ionospheric density depletion that is moving in southward direction. The ‘depletion wall’ is somewhat similar in shape to the one observed in the April 2000 storm (Fig.7-1) but is different from the other one observed on 29 October 2003 in the Washington area (Fig.7-5). The ionospheric delay drop in Europe appears to be less pronounced than the drop observed in the American sector. This can be explained with the differences in both, the local time and the latitude. It is well known that the ionospheric behaviour and effects exhibit substantial spatial and temporal variations, both during quiet and disturbed geomagnetic conditions.

To further explain the observed difference let's have a more detailed look at the development of this particular storm. In general, the geomagnetic storm impact is expected first on the high-latitude ionosphere because the latter is much stronger coupled with the magnetosphere and the solar wind. High-latitude electric fields, precipitation of energetic particles, and plasma convection, are reportedly the most powerful driving forces for the highly dynamic and complex processes in this region. During the onset phase of a storm, rapid ionization changes are generated over the polar regions leading to significant increase and variability of the plasma density. Thus, large ionospheric plasma density gradients are formed which, in general, propagate in equator-ward direction. In the case of the geomagnetic storm of 29 October 2003, on the background of already increased TEC, a patch of even higher ionization was detected at about 0700UT (Fig.7-9). The patch grew in size and moved southward over both the day-time and night-time hemispheres. The gradients are obviously larger in the sunlit hemisphere which explains the more pronounced ionospheric delay depletion in the American sector at around 2100UT.

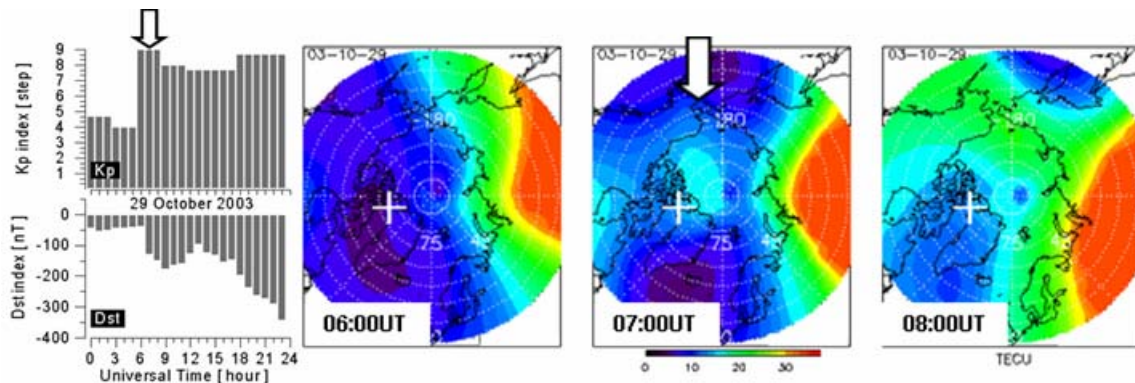


Fig.7-9. Ground-based GPS TEC observation of the North Pole region for the ionospheric storm events that started on 29 October 2003 (*Stankov et al., 2006*). The geomagnetic pole is marked with a cross.

Further to our analysis of the ionospheric delay profiles, we have also calculated the slant TEC differences between the TEC values obtained at the reference station BRUS and the TEC values obtained at the other 4 stations (Fig.7-10). The results, also obtained from measurements along links to satellites 21 and 17, are consistent with the just presented results for the ionospheric delays. The latitudinal gradients are clearly seen on the plots for DOUR and BREE. Since the latitudinal difference between BRUS and DENT is negligible, there is no significant difference in their measurements of the TEC.

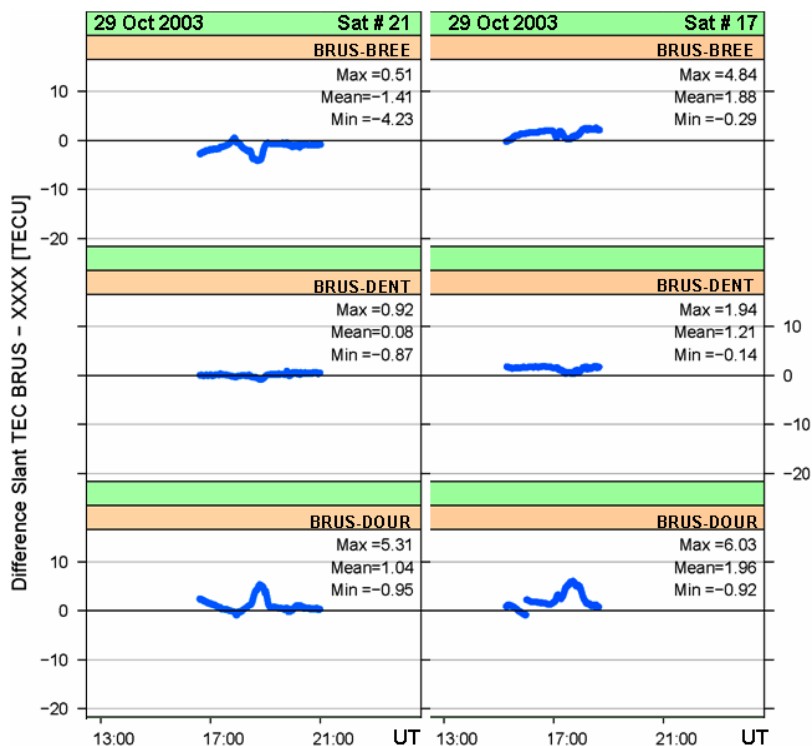


Fig.7-10. Slant TEC differences between BRUS and 3 other stations during the storm of 29 October 2003 as measured via GPS satellites No.21 (left) and No.17 (right).

7.1.2 The ionospheric storm on 20 November 2003

Another severe geomagnetic storm started in the early hours of 20 November 2003, with Kp increasing to almost maximum value in the afternoon hours, and Dst values reaching the -400 nT mark in the early evening hours (Fig.7-11).

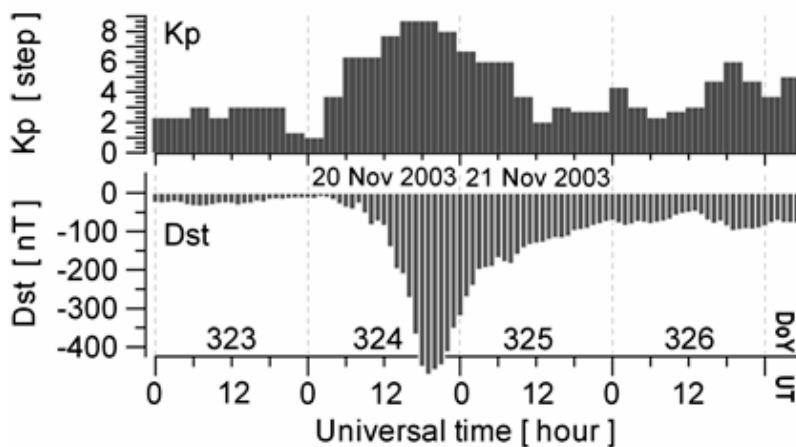


Fig.7-11. The 20-21 November 2003 ionospheric storm background as represented by the planetary geomagnetic indices Kp (top panel) and Dst (bottom panel).

Again, large ionospheric gradients (‘depletion walls’) (left panel) observed among CORS clusters in the Ohio area (right panel) on 20 November 2003. The ionospheric gradient is shown crossing the station GUST, then GARF, WZOB, then TIFF (Fig.7-12). The GARF to WZOB gradient was estimated to be about 20 m in 50 km distance (i.e. 400 mm/km) and the speed of the wall was estimated at about 250 m/s (*Dehel et al.*, 2004).

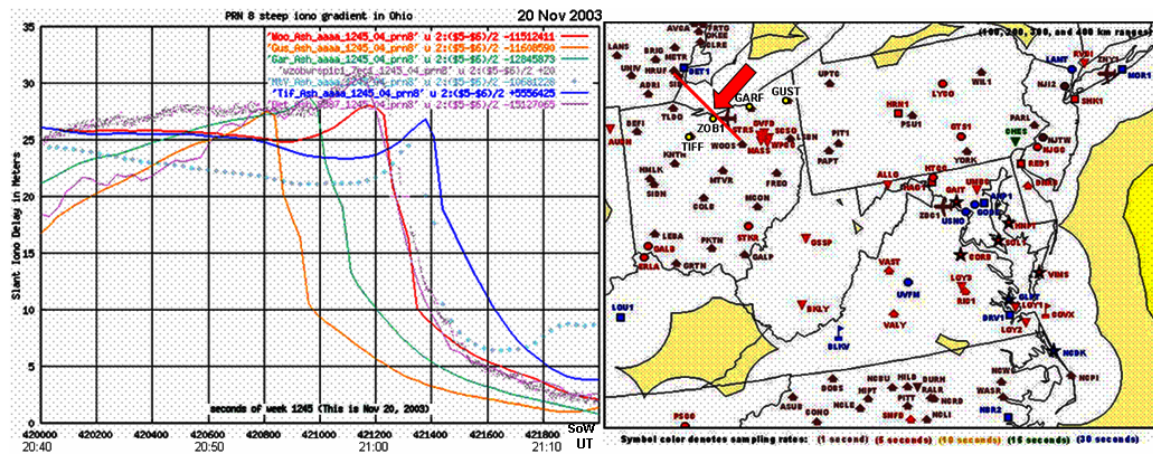


Fig.7-12. Large ionospheric gradients (‘depletion walls’) (left panel) observed among CORS clusters in the Ohio area (right panel) on 20 November 2003.

Similarly to the case of the 29 October 2003 storm, we have analysed all available observations from the selected network of GPS stations in Belgium during the storm of 20 November 2003. The ionospheric delay measurements deduced from all satellite links on this day are plotted in the upper panel of Fig.7-13, again with references to the corresponding ionospheric piercing points given in the bottom panel. The figure clearly shows the sharp increase of the ionospheric delay soon after the onset of the storm followed by a sharp decrease during the ‘negative phase’ of the storm. Very interesting is the period of major perturbations of the delay in the evening period between 1700 and 2300 UT. We will turn our attention to this particular period with the intention of finding steep density gradients and ‘irregularity walls’.

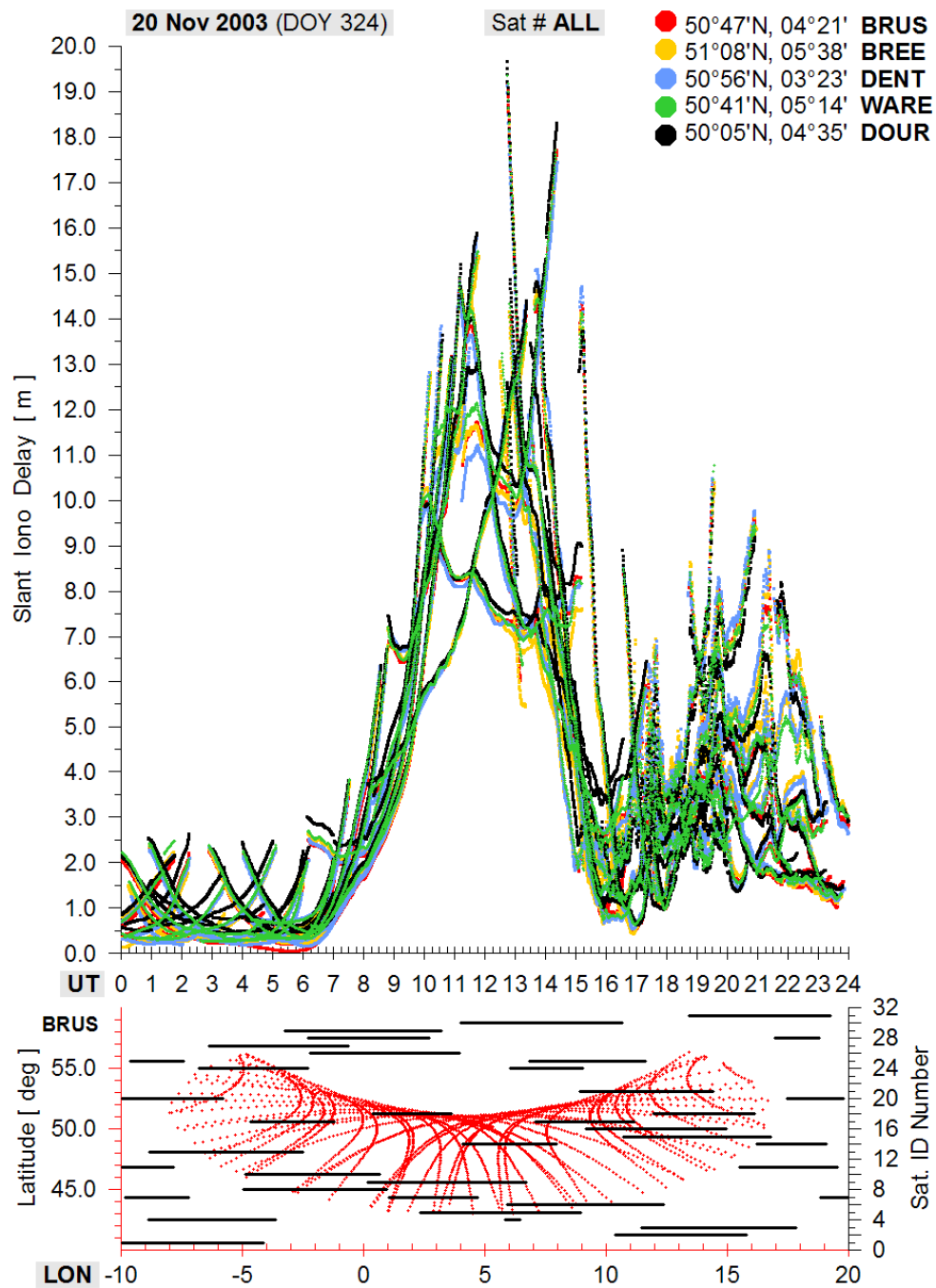


Fig.7-13. Ionospheric delays during the storm of 20 November 2003 measured via the GPS satellites ‘visible’ from the selected GPS stations in Belgium (top panel). The satellite IPP traces over Europe (with reference to the base reference station BRUS) are plotted in the bottom panel with red colour. The period of ‘visibility’ of each GPS satellite, again with reference to the BRUS station and according to UT, is plotted in the bottom panel with black solid lines.

The task is again complicated due to the great variability in satellite IPP trace shapes and orientations (**Fig.7-14**, left). Although the decrease of the ionospheric delay in the afternoon hour is clearly visible, the magnitude of the decrease and the speed of this decrease vary significantly from link to link. Notice how, despite the time coincidence of satellite visibility, the measurements along the link to satellite #30 deviate significantly from the measurements based on other satellite links. It confirms again the importance of proper consideration of the IPP trace characteristics. As mentioned above, the attention is on the 1700 to 2300 UT period. The link to satellite #15 reveals a substantial increase in the delay followed by a sharp increase about 30 minutes later (**Fig.7-14**, right). Unfortunately, the link has been closed before eventually determining whether this had been a manifestation of an irregularity wall or not.

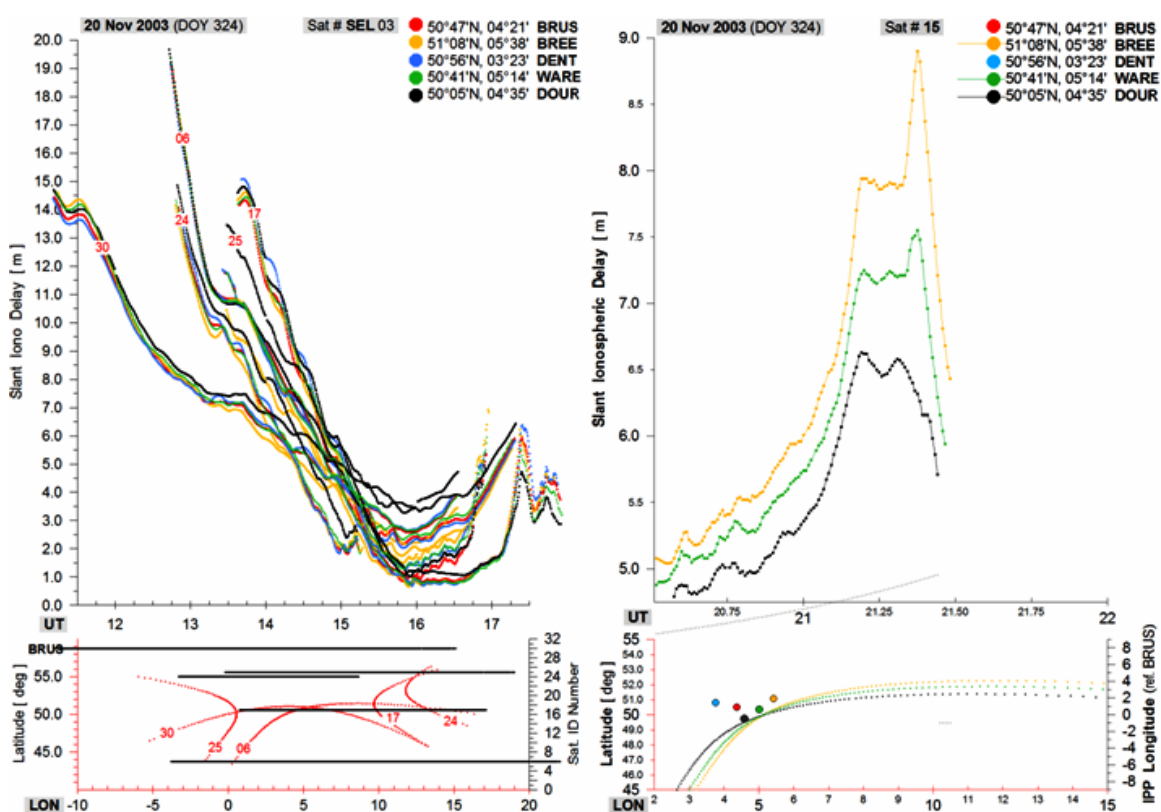


Fig.7-14. Ionospheric delays during the storm of 20 November 2003 as measured via GPS satellite selection #3 (6, 17, 24, 25, 30) (left) and satellite No.15 (right).

Other links have been analysed for the same period and two of the links, to satellites #11 and #31, revealed a possible existence of a moving ‘irregularity wall’ (**Fig.7-15**) similar to the one observed in the American sector at approximately the same time. The wall is of relatively modest magnitude, further decreasing while travelling southward.

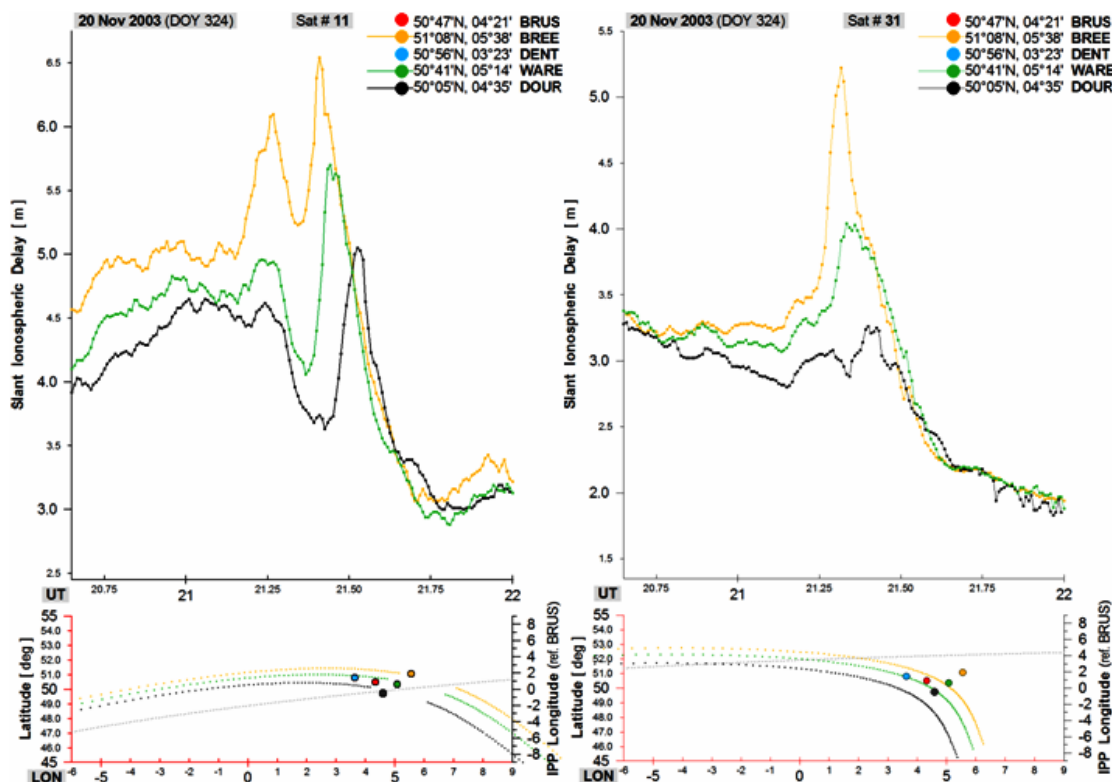


Fig.7-15. Ionospheric delays during the storm of 20 November 2003 as measured via GPS satellites No.11 (left) and No.31 (right).

The calculated slant TEC differences between BRUS and other stations are again consistent with the slant delay results (Fig.7-16). Latitudinal gradients, appearing with opposite signs are visible on the plots for DOUR and BREE.

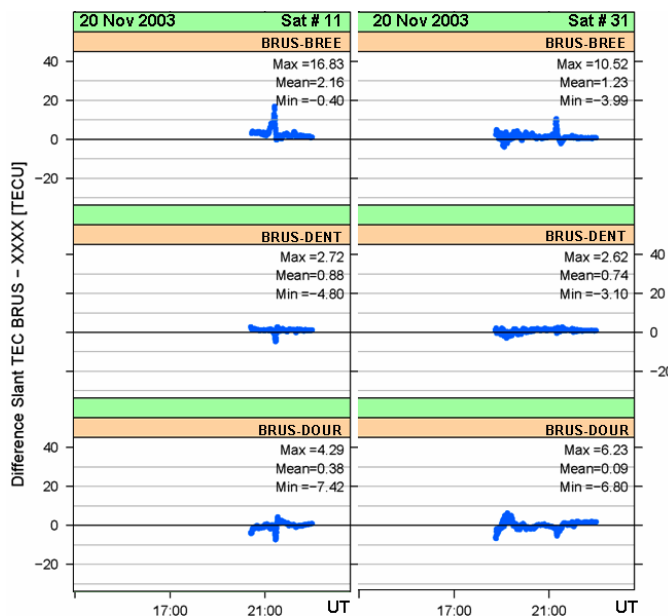


Fig.7-16. Slant TEC differences between BRUS and 3 other stations during the storm of 20 November 2003 as measured via GPS satellites No.11 (left) and No.31 (right).

7.2 *Future work*

The analysis in the previous section raises some important questions that need to be addressed in further investigations.

It is generally accepted that the large variety of irregular ionospheric structures falls into two major categories: those produced by rapid changes of thermospheric composition (or alternatively, induced by large-scale electrodynamic drifts), and the others, well known as Travelling Ionospheric Disturbances (TIDs). Although not exclusively, ionospheric gradients showing preferences to NE-SW and SE-NW directions are known to characterize propagation of middle-scale TIDs. In this sense, it is very important to investigate whether TIDs may also be held responsible for the observed moving ionospheric features.

Another question is whether ionospheric irregularities, occurring outside the geomagnetic storms, are capable of generating ionospheric features similar to those reported here. Recently, ionospheric irregularities have been estimated on a global scale by using ionospheric radio occultation (IRO) measurements (*Stankov et al.*, 2006). Results show that the occurrence frequency is higher during day and lower during night. Also, it has been found that the intensity of the ionospheric irregularities increases sharply during winter.

There is also a methodological issue concerning the research of the ionospheric anomaly phenomena. The approach used here involves a due consideration of various details such as the ground station locations, the shape and orientation of the satellite IPP traces. The task is quite demanding and is prone to omissions and misinterpretation of some observations. For better results, it will be necessary to involve more sophisticated ray tracing algorithms. Automation of the analysis is also a must. Another obvious candidate for monitoring and investigating ionospheric anomaly phenomena is the TEC mapping. On the one hand, the TEC mapping provides opportunities for covering larger areas thus allowing for easier detection and analysis of dynamic ionospheric structures. On the other hand, since TEC values at grid points are mostly obtained by interpolating between measured values, TEC gradients obtained in this way may smooth out the real gradients and thus deem the interpretation incorrect. Therefore, TEC mapping should be made with very high spatial and temporal resolution and for aviation purposes, it should be provided in real time. It is expected that a combined approach would bring more reliable and timely results.

8 CONCLUSIONS

An analysis of the positioning error due to the ionosphere has been done considering typical ionospheric conditions: quiet ionosphere, medium-amplitude TID, large-amplitude TID and geomagnetic storm.

In section 4, we analyzed in details the different time intervals chosen in WP 220 (see section 5). These time intervals of 15 minutes (except for the quiet day) were chosen on the basis of RoTEC values (obtained with the one-station method) and are representative of the different typical ionospheric conditions mentioned above. We obtained values of the positioning error due to the ionosphere for each component (north, east, up) and extracted the maximum values for the considered periods. However, because of the small amount of data (only 15 minutes per day), these values cannot be considered as representative for the whole duration of the studied phenomenon. Nevertheless, this analysis showed that the baseline orientation influences the values of the positioning error. Moreover, we observed that the positioning error was also very different from a component to another (north, east, up).

In section 5, we have studied the correlation between the ionospheric residual term $I_{AB,GF}^{ij}$ and the positioning error due to ionosphere when considering all the available data (i.e. 24 hours) for the 4 days studied in section 4. The main conclusion is that there is a positive correlation between the variability of $I_{AB,GF}^{ij}$ and the positioning error due to ionosphere: larger variability in $I_{AB,GF}^{ij}$ is followed by larger positioning errors. The largest effects were observed during the occurrence of the geomagnetic storm where the positioning error due to ionosphere reached 80 cm. The maximal values of this error observed for TID's were 15 cm and 22 cm, respectively for the medium-amplitude TID and the large-amplitude TID. During quiet days in terms of ionospheric variability, the positioning error due to ionosphere is typically 1-2 cm but reached 5 cm, which is still within the usual RTK accuracy level. In this section, we have also observed that there is a relationship between the baseline length and the effects on positioning: positioning error due to ionosphere increases with increasing baseline length. In addition, for a given ionospheric disturbance, the positioning error due to the ionosphere depends very much on baseline orientation. These two results mean that the implementation of a Galileo Local Component for the monitoring of ionospheric threats would require the use of all available Belgian Dense Network station in order to provide users with reliable information.

In section 6, we analyze the contribution of small-scale tropospheric structures (detected using the Ionospheric-free double difference Index developed in WP 250) to the RTK error budget. We found that, in most of studied cases, IF DD Indexes larger or equal to 5 (the so-called "5+" category in WP 250) are the origin of degradations in positioning errors which range between 20 cm and 40 cm even on short baselines (35 cm on BREE-MEEU (7 km) and 31 cm on BRUS-GILL (4 km)). Nevertheless, it appears that, on

baselines larger or equal to 20 km, it is not always possible to extract the contribution of small-scale tropospheric structures to the positioning error from the “background” positioning error due to other sources as residual multipath, noise, constellation geometry, ... Again, this result means that the implementation of a Galileo Local Component for the monitoring of tropospheric threats would require the use of all available Belgian Dense Network stations. In the Northern part of the BDN, typical baseline length is of the order of 20 km what can be considered as the upper limit in order to be able to extract some information about positioning error due to small-scale tropospheric structures. In the Southern part of the BDN, baselines lengths can reach 30-35 km what is too large in order to extract quantitative information, at least at the present time.

The establishment of correct statistical correlation between our activity indexes (ionosphere and troposphere) and the RTK positioning error would require the analysis of larger data sets. Unfortunately, the software used in this WP is not yet fully operational. On the one hand, our results still contain unexplained peaks which could be due to unfixed bugs but also to satellite geometry or other “physical” effects. Further investigations are necessary to understand these phenomena. On the other hand, a few parts of our positioning software are yet not fully automated (mainly ambiguity resolution). As a consequence, the software cannot be run on larger data sets at the present time.

In section 7, we analyse local TEC behaviour induced by the storms of 29 October 2003 and 20 November 2003 which could pose a threat for applications in aviation. It has been found that moving ionospheric ‘irregularity walls’ did occur in Europe during these storms although not so pronounced as in the American sector. Further investigations are needed with data from other major geomagnetic storms.

REFERENCES

- Dehel, T., Lorge, F., Warburton, J., Nelthropp, D. (2004): *Satellite navigation vs. the ionosphere: where are we, and where are we going?* Proc. ION GNSS, September 21-24, 2004, Long Beach, CA.
- Joosten, P., Tiberius, C., 2000. Fixing the Ambiguities: Are You Sure They're Right? GPS World, 11 (5), pp 46-51.
- Leick, A., 2004. GPS Satellite Surveying 3rd Edition. John Wiley & Sons, New York, 435p.
- Luo, M., Pullen, S., Dennis, J., Konno, H., Xie, G., Walter, T., Enge, P., Datta-Barua, S., Dehel, T. (2003): *LAAS Ionosphere Spatial Gradient Threat Model and Impact of LGF and Airborne Monitoring*. Proc. ION GPS 2003, Portland, OR, Sept. 9-12, 2003.
- Murphy, T., Harris, M. (2006): Mitigation of ionospheric gradient threats for GBAS to support CAT II/III. ION meeting, 26-29 September 2006, Forth Worth, TX, USA
- Seeber, G., 2003. Satellite Geodesy Second Edition. de Gruyter, New-York, 589 p.
- Stankov, S. M., Jakowski, N., Tsybulya, K., Wilken, V. (2006): *Monitoring the generation and propagation of ionospheric disturbances and effects on GNSS positioning*. Radio Science, Vol.41, No.5, RS6S09, (doi:10.1029/2005RS003327).
- International GNSS Service (IGS): <http://igsceb.jpl.nasa.gov>